Applied Magnetic Resonance (2023) 54:1099–1133
https://doi.org/10.1007/s00723-023-01579-y

Applied
Magnetic Resonance

REVIEW

Morphology of Industrially Relevant Polymers by ^{1}H NMR Spin-Diffusion

V. M. Litvinov[1,2] · **Yongfeng Men**[2,3]

Received: 24 April 2023 / Revised: 20 July 2023 / Accepted: 21 July 2023 /
Published online: 1 September 2023

Abstract

Applications of time-domain ^{1}H NMR spin-diffusion experiments for studying morphology of industrially relevant polymers are reviewed. The method exploits the contrast in molecular mobility in different phases in multi-phase organic materials, which could be in some cases advantageous to traditional morphological methods. A brief overview of different time-domain spin-diffusion methods and data analysis is provided. The effect of domain size distributions and their clustering, which were previously analyzed by numerical simulations of spin-diffusion curves, is discussed. Examples of different types of morphology in polymers with hard and soft domains are presented, namely, lamellar morphology and its changes during annealing; interfacial layers in different types of polymers; fragmented structure of crystal lamellae in isotactic polybutene-1 and its copolymer with form I crystals; fibrillar morphology of melt-spun Nylon 6 and poly(ethylene terephthalate) fibers; morphology of gel-spun ultra-high-molecular-weight polyethylene fibers; ionic clusters in polymeric ionomers; the rubber–filler interface in filled rubbers; the structure of network of physical junctions in filled rubbers and ionomers; and morphology of thermoplastic polyurethanes. Domain sizes from the NMR method are compared with those determined for the same materials by small-angle X-ray scattering and transmission electron microscopy. All results are in good agreement. In addition to domain sizes, the NMR method provides several details of polymer morphology, namely, morphological heterogeneities, the type and the thickness of interfacial layers, the presence of (sub)nano-domains, and molecular mobility in different phases. Thus, the method offers information that is complementary to the conventional methods. The effect of structural heterogeneities on macroscopic properties is briefly discussed.

In honour of Prof. Bernhard Blümich on the occasion of his 70th birthday.

Extended author information available on the last page of the article

1 Introduction

The type of phases and their mutual arrangements in materials, as commonly called morphology, play a large role in determining a wide range of bulk properties of polymeric materials [1]. The type of morphology in homopolymers and polymeric blends is a result of several aspects, namely the polymer thermodynamics that depends on the chemical structure of polymer chains; the composition of multicomponent materials; the crystallization rate, and glass transition temperature (T_g) of components in polymer blends and block copolymers; processing conditions; and several other factors. Semicrystalline polymers belong to the largest class of synthetic polymers. An increase in the number of comonomer units in polymer chains causes changes in the morphology of melt-crystallized polymers from the spherulitic morphology with polymer chains aligned in lamellar crystals within spherulites, to granular-based morphology and fringed micelle-like structures at a large number of comonomer units if they cannot be built-in crystals [2]. Drawing of semicrystalline polymers causes a change of the spherulitic morphology into the fibrillar morphology [3]. A wide variety of morphologies is observed in block copolymers, namely the lamellar morphology, morphologies with cylindrical, spherical, cubic, gyroid, and several other geometries of domains [4]. Different morphological structures are observed in polymeric blends, ionomers, and other polymeric materials.

A large number of methods have been used to give insights into the shape and dimensions of domains that are formed by different phases in polymers. [5–9] The most widely used methods are transmission electron microscopy (TEM), scanning electron microscopy (SEM), and several other microscopy methods. These methods commonly provide two-dimensional projections that represent morphology through the entire thickness of thin slices that are cut by a microtone method, or surface morphology of polymers. This information could be influenced by the preparation of microtome slices that are usually stained with heavy metals or chemically etched. The sample preparation might also affect morphology and the contrast to different morphological elements. A thorough analysis of microscopy images is used for the reconstruction and visualization of three-dimensional (3D) morphology [10]. Small-angle X-ray scattering (SAXS) and neutron scattering (NS) experiments are free from elaborated sample preparations and provide the average over the entire sample morphological information. [11–13] For semicrystalline polymers, these methods determine the thickness of crystalline and amorphous domains, their distributions, as well as the crystal perfection by wide-angle X-ray diffraction (WAXD). Domain size determination by SAXS can be performed for well-ordered systems with the long-range periodicity of domains that have high- and low-electron densities. Quantitative interpretation of the scattering data requires knowledge of the type of morphology for selecting a theoretical model for the data analysis [14]. The size of tiny crystals can be also estimated from the width of WAXD peaks [15]. Another method that provides volume-average domain sizes is NMR spin-diffusion or magnetization transfer experiments [16, 17]. A broad range of phase dimensions ranging from 0.1 nm to about 200 nm can be determined by this method. The method is also capable of determining the size of interfaces at the length scale where other

methods fail due to a lack of contrast or a small length scale of nanoscale heterogeneities. Different spectroscopy imaging methods and magnetic resonance imaging (MRI) provide information that is complementary to TEM, SEM, SAXS, and NMR spin-diffusion methods. These methods offer the contrast to concentration gradients, chemical composition, orientation, and some other material heterogeneities [18–22]. However, these methods have a lower spatial resolution. Last but to least, atomic force microscopy (AFM) offers high-resolution images of surface structures ranging from nanometers to hundreds of micrometers [8, 23].

2 Domain Size Determination in Hard–Soft Organic Materials by ^{1}H Time-Domain NMR Spin-Diffusion Experiments

The spin-diffusion is an exchange of the longitudinal (spin–lattice) magnetization between different phases that is observed if their magnetization is not distributed evenly. The process takes place on a mesoscopic scale and is facilitated by the dipolar couplings of abundant nuclear spins. The spin-diffusion process is analogous to heat conductivity between different bodies in the presence of a temperature gradient. The determination of domain sizes in hard–soft organic materials by ^{1}H NMR spin-diffusion experiments requires the following four steps: (1) an optimization of a dipolar filter to obtain its highest selectivity for the polarization of nuclei spins in one of the phases; (2) the knowledge of the spin-diffusion coefficient for different phases which is needed for a calculation of domain sizes; (3) the proper choice of a model that describes the morphology of studied material; and (4) the appropriate solution of the spin-diffusion equations for specific morphology with the corresponding initial and boundary conditions. A wide variety of NMR spin-diffusion experiments are used for studying morphological heterogeneities in materials [17, 24–27]. One- and two-dimensional spin-diffusion experiments are performed in the frequency- and time domains on various nuclei with high-field NMR spectrometers. The proton spin-diffusion process is very frequently utilized for domain size determination because of the high sensitivity of proton NMR and effective spin-diffusion process among protons. Spin-diffusion studies are often performed with signal detection in the time-domain on low-field NMR relaxometers.

The time-domain NMR (TD-NMR) and wide-line NMR spin-diffusion methods can be applied to multi-phase materials composed of domains with significantly different molecular mobility and, consequently, with significant differences in the strength of the dipole–dipole interactions in the phases/components. In all experiments, a gradient of the longitudinal magnetization is created by exploiting selective relaxation experiments or excitation of the magnetization in one of the phases/domains, which is followed by recording the equilibration of spatially heterogeneous magnetization through the sample volume as a function of time. Three types of dipolar filters are used in TD-NMR spin-diffusion experiments: a double-quantum (DQ) dipolar filter [28–30], the Goldman–Shen filter [31], and a magic-and-polarization echo (MAPE) filter [25, 32]. The DQ dipolar filter offers high selectivity for the polarization of the magnetization in either rigid or soft phases [33].

Domain size determination requires knowledge of the type of morphology. An approximation of the lamellar morphology, and morphologies with cylindrical and spherical domain shapes is often used for the analysis of spin-diffusion curves. An example of spin-diffusion curves, which present change in the relative intensity of the longitudinal magnetization in the crystalline phase, crystal–amorphous interface, and the amorphous phase against the square root of spin-diffusion time, is shown for poly(butene-1)-ethylene random copolymer with form I' crystals and the lamellar morphology (Fig. 1) [34]. The magnetization in the crystalline phase is selectively polarized with a DQ dipolar filter. As shown in Fig. 1, the relative fraction of the relaxation component of the crystalline phase (black points) decreases with increasing spin-diffusion time, t_{sd}, and the signal intensity for the crystal–amorphous interface (red points) and the amorphous phase (blue points) increases. The sigmoidal shape of the spin-diffusion build-up curve for the amorphous phase at short t_{sd} is common for semicrystalline polymers, block copolymers, and polymeric blends with an interface that separates different phases [25, 28, 32]. In the presence of the crystal–amorphous interface, the magnetization flows first from the crystalline phase into the interface, and with a delay into the amorphous phase (Fig. 1). At short spin-diffusion times, the relative intensity of the interface fraction increases due to the magnetization transfer from crystal lamellae to the interface, whereas its value

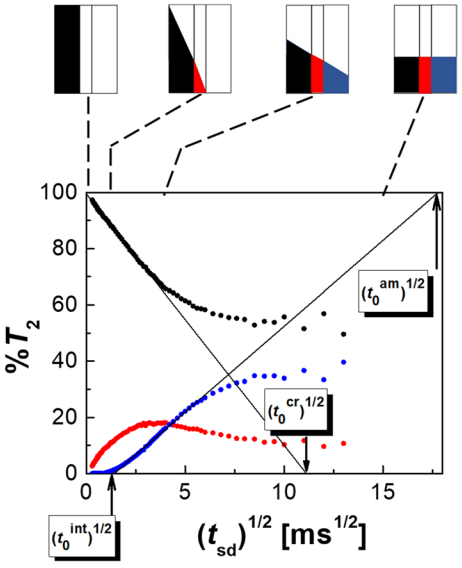

Fig. 1 Spin-diffusion build-up and decay curves for poly(butene-1)-ethylene random copolymer with form I' crystals and lamellar morphology. The magnetization of the crystalline phase was selected by a DQ dipolar filter. The curves for the crystalline phase, the crystal–amorphous interface, and the amorphous phase are shown by black, red, and blue points, respectively. Lines show the slope of the spin-diffusion curves in the initial spin-diffusion time regime. Their extrapolation to the *x*-axis provides intercept values $(t_0^{index})^{1/2}$, which are used for the estimation of domain sizes. The schematic drawing on the top shows the magnetization flow: the crystalline phase → the crystal–amorphous interface → the amorphous phase and, finally, the equilibration of the magnetization through the sample volume [34] (color figure online)

decreases at longer t_{sd} due to the magnetization flow from the interface to the amorphous phase (Fig. 2).

A simple method is often used for the calculation of domain sizes under the suggestion of the lamellar, cylindrical, or spherical types of morphology [24, 34–39]. For ill-defined morphologies, this analysis provides (i) the shortest distance across domains if domains have a smooth surface; or (ii) the volume-to-surface ratio of domains in the case of a very rough surface. The use of this method for the lamellar morphology is illustrated in Fig. 1. The extrapolation to the *x*-axis of the initial slope of the dependence for the magnetization source (the crystalline phase) provides the intercept $(t_o^{cr})^{1/2}$. Its value can be considered a measurable quantity for the rate of the magnetization exchange between crystal lamellae and interlamellar amorphous domains (the sink) through the shortest distance across the lamellar structure [40]. Deviation from the linear behavior at long spin-diffusion times can originate from several reasons [24–26, 34]. It is often caused by a change in the dimensionality of the spin-diffusion process due to the shape of domains (e.g., spin-diffusion in the direction perpendicular to lamellar thickness causes deviation from one-dimensional spin-diffusion model); by distribution in phase dimensions, irregularities in domain positions, and/or roughness of

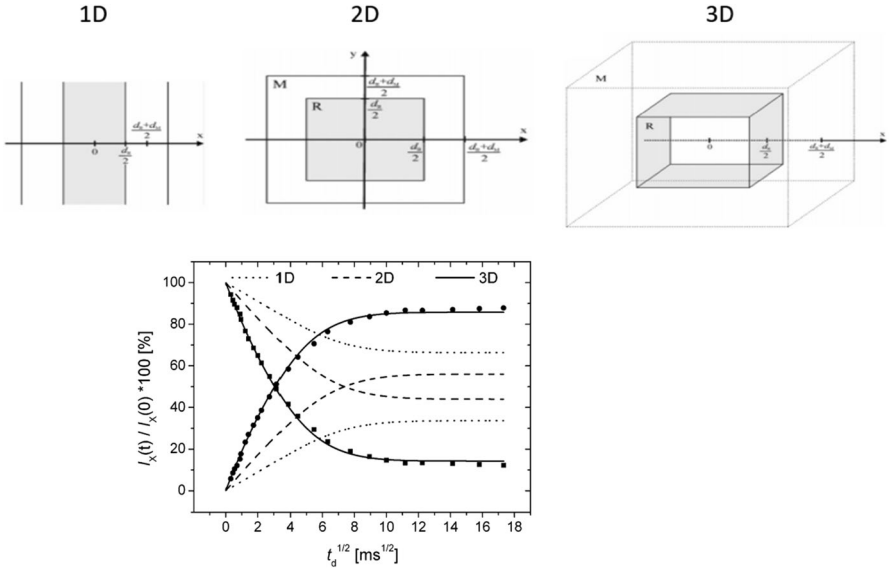

Fig. 2 Proton spin-diffusion decay and build-up curves (points) for rigid (*R*) and soft (*M*) domains in thermoplastic polyurethane (TPU) with 45% of hard segments. The magnetization of rigid domains was selected by a DQ dipolar filter. The lines correspond to the data fit with 1D, 2D, and 3D solutions of the spin-diffusion equations [46]. It is noticed that simulated curves should reach the same value for the 1D, 2D, and 3D solutions. Apparently, the authors of the study made a mistake in the curves' normalization. It is also noticed that the asymptotic value of the normalized signal intensity for rigid domains in the TPU is more than two times smaller than the weight fraction of hard domains. This is due to smaller proton density in hard domains and, possibly, also due to the T_1 effect that was not discussed in the publication

domain surface. The intercept method can be used if the spin-diffusion rate is significantly faster than the rate of spin–lattice (longitudinal) relaxation (T_1 relaxation). The size of domains is calculated from the intercept value t_o according to the equation

$$d_{\text{source}} \approx \frac{4\varepsilon}{\sqrt{\pi}} \frac{\rho_{\text{sink}}}{\rho_{\text{source}}} \sqrt{D_{\text{eff}}} \sqrt{t_0}. \tag{1}$$

Here, the dimensionality of the spin-diffusion process is characterized by ε. Value of ε equals 1, 2, and 3 for lamellar morphology, cylindrical, and spherical shape of domains, respectively. ρ_{index} is the specific density of the source and the sink phases. D_{eff} is the effective spin-diffusion coefficient that is calculated using spin-diffusion coefficients for the source and sink phases with Eq. 2

$$\sqrt{D_{\text{eff}}} = \frac{\sqrt{D_{\text{source}}}\sqrt{D_{\text{sink}}}}{(\sqrt{D_{\text{source}}} + \sqrt{D_{\text{sink}}})/2}. \tag{2}$$

The use of D_{eff} causes an overestimation of crystal size and rigid domains in two-phase polymers, since the longitudinal magnetization will diffuse faster within crystals as compared to the average of the diffusivities—D_{eff}, whereas the size of soft domains will be underestimated. It is noted that an error in values of D_{eff} does not largely affect the accuracy of domain size determination, since the square root of the spin-diffusion coefficients is used in Eq. 1. An approximate size of the interface on the lamellar surface can be obtained from the intercept $(t_o^{\text{int}})^{1/2}$ that is shown in Fig. 1. Estimated interface thickness is also not very sensitive to the value of D_{eff} [25]. Thickness of interlamellar amorphous layers is estimated from value of $(t_o^{\text{am}})^{1/2}$—$(t_o^{\text{int}})^{1/2}$.

A few methods were used to determine the spin-diffusion coefficient for rigid and soft domains. To a good approximation, the spin-diffusion coefficient D can be determined from the line width at its half-height $\Delta\nu_{1/2}$ for the rigid and soft phases using Gaussian and Lorentzian approximations of the line shapes in wide-line NMR spectra, as shown by Eqs. 3 and 4 [25]

$$D_{\text{rigid}} \approx \frac{1}{12}\sqrt{\frac{\pi}{2ln2}}\langle r^2\rangle \Delta\nu_{1/2} \tag{3}$$

$$D_{\text{soft}} \approx \frac{1}{6}\sqrt{\frac{\pi}{2\ln 2}}\langle r^2\rangle \Delta\nu_{1/2}, \tag{4}$$

where $\langle r^2 \rangle$ is the mean square distance between the nearest nuclear spins. Using these equations, spin-diffusion coefficients for the crystalline phase (D_{cr}), crystal–amorphous interface (D_{int}), and the amorphous phase (D_{am}) were determined for HDPE [41] and iPP [38]. The spin-diffusion coefficient for all these fractions of HDPE and iPP decreases with increasing temperature due to an increase in molecular mobility and the thermal expansion causing an increase in interchain distances. In the studied temperature range, values of D_{cr}, D_{int}, and D_{am} for HDPE are in the

range of 0.39–0.27, 0.27–0.15, and 0.15–0.07 nm^2/ms, respectively. Similar values of the spin-diffusion coefficients were determined for PA6 fibers [28, 32].

The spin-diffusion coefficient for rigid phases can be estimated from the second van Fleck moment (M_2) of NMR line in wide-line NMR spectra

$$D_{\text{rigid}} \approx \frac{1}{6}\sqrt{\pi}\langle r^2\rangle\langle M_2\rangle. \tag{5}$$

M_2 for crystalline phases can be also determined from the a and b shape parameters of the Abragamian function (Eq. 6) that describes well the free induction decays (FID) of crystals: $M_2 = a^2 + b^2/3$ [42]

$$A(t) = A(0)\exp\left(-\frac{a^2t^2}{2}\right)\sin(bt)/bt. \tag{6}$$

Spin-diffusion coefficients are most often estimated by a calibration method using model compounds with known shapes and the size of domains that are determined by scattering or microscopy methods [17, 40]. In this method, the best-fit values of D are obtained by analyses of spin-diffusion curves using known domain sizes. The number of variables in the analysis can be reduced using the proton spin density that is determined by molecular modeling [43]. It was also shown that spin-diffusion coefficients can be correlated with the rate of the transverse magnetization relaxation [40]. Empirical equations were proposed to estimate spin-diffusion coefficients from T_2 value of polyisoprene (PI) and polystyrene (PS) domains in PI-PS block copolymers and blends using Eqs. 7 and 8

$$D = \left(4.4\cdot 10^{-5}T_2^{-1} + 0.26\right)\ \text{nm}^2/\text{ms}\ \left(\text{valid for } 1000\ \text{Hz} < T_2^{-1} < 3500\ \text{Hz}\right) \tag{7}$$

$$D = \left(8.2\cdot 10^{-6}T_2^{-1.5} + 0.007\right)\ \text{nm}^2/\text{ms}\ \left(\text{valid for } 0 < T_2^{-1} < 1000\ \text{Hz}\right). \tag{8}$$

The T_2 value in the equations is in sec. The authors of the PI–PS study overlook a mistake in Eq. 7 in proof of their paper. Correct Eq. 7 was provided in Fig. 4a in the PI–PS study [40], and in the present paper.

The effective spin-diffusion coefficient for interfaces can be estimated from the equation above and the population-average T_2 value of the interface (T_2^{int}) that is calculated from T_2 of rigid (T_2^{rigid}) and soft (T_2^{soft}) domains as follows:

$$1/T_2^{\text{int}} = f^{\text{rigid}}/T_2^{\text{rigid}} + f^{\text{soft}}/T_2^{\text{soft}}, \tag{9}$$

where $f^{\text{rigid}} + f^{\text{soft}} = 1$, and f^{rigid} and f^{soft} are the fractions of these domains.

Spin-diffusion coefficients were also directly calculated independent of the calibration method as follows. A series of solid-state, high-field 2D ^{1}H-^{13}C solid-state HETCOR NMR experiments with different ^{1}H–^{1}H spin-diffusion periods were recorded for amorphous polymeric materials [44]. Then, spin-diffusion coefficients for different phases were calculated from the results of the 2D NMR experiments and internuclear distances that were determined by energy-minimized chain dimension simulations with molecular modeling. The intra- and

interchain spin-diffusion coefficients may be separately determined, too. The proton spin-diffusion coefficient for crystalline materials was also directly calculated from the known structure of the crystal lattice using the first-principles simulations [45].

After spin-diffusion coefficients have been determined, one of the following methods is used for determining domain sizes: (1) the intercept method as described above; (2) a rigorous analysis of spin-diffusion curves using general analytical solutions of spin-diffusion equations for defined morphologies; or (3) numerical simulation of spin-diffusion curves for more complex morphologies.

General analytical solutions of spin-diffusion equations, which describe the magnetization transfer between different domains, can be obtained using a diffusion equation

$$\partial M(r,t)/\partial t = N[D(r,t)\, NM(r,t), \tag{10}$$

where M (r, t) is the time- and spatially dependent longitudinal magnetization, and D (r,t) is the spatially dependent spin-diffusion coefficient. The spin-diffusion equation describes the irreversible spatial propagation of the magnetization in the limit of isotropic spin-diffusion. Details on the morphology of multi-phase polymers are provided by a fitting of the entire spin-diffusion curves with solutions of this partial differential equation. Several types of morphology were analyzed with one-dimensional (1D), 2D and 3D spin-diffusion processes for two- [25, 46] and three-phase polymers [24, 32]; three-phase cylindrical morphology [47]; fibrillar morphology in polymeric fibers [28]; and some other types of morphology. Figure 2 shows calculated spin-diffusion curves for 1D, 2D, and 3D morphologies in a two domains system [46]. The analyses shows that 3D morphology describes well the experimental data for thermoplastic polyurethane.

Figure 3 shows the effect of the interface thickness on the simulated decay and build-up spin-diffusion curves for rigid- and soft domains, respectively [32]. The transfer of the magnetization from rigid to soft domains is delayed in the presence of the interfacial layer between these domains. The delay increases with increasing the interface thickness. The initial slope of the dependence of the magnetization increase for soft domains provides the intercept value $(t_o)^{1/2}$ that is used for the calculation of the interface thickness from Eq. 1 and D_{eff} value.

Numerical simulations of spin-diffusion curves were used for studying more complex morphologies. This method can provide fine details of morphology in multi-phase polymers. Non-ideal, modestly periodic morphologies cause slower decay of spin-diffusion curves for the source of the magnetization [48]. Qualitatively, this is the signature of a distribution of domain sizes. The initial slope of the spin-diffusion curves is a measure of small domain sizes, whereas larger domains and their spatial distribution determine the spin-diffusion rate at the longer spin-diffusion times [26, 48, 49]. The effect of domain size distribution and domain clustering on spin-diffusion curves was demonstrated by numerical simulations (Figs. 4, 5, 6) [49, 50]. The magnetization decay and recovery curves approach the equilibrium state more gradually with increasing clustering of domains. Dynamic heterogeneities, the roughness of the interface surface, and

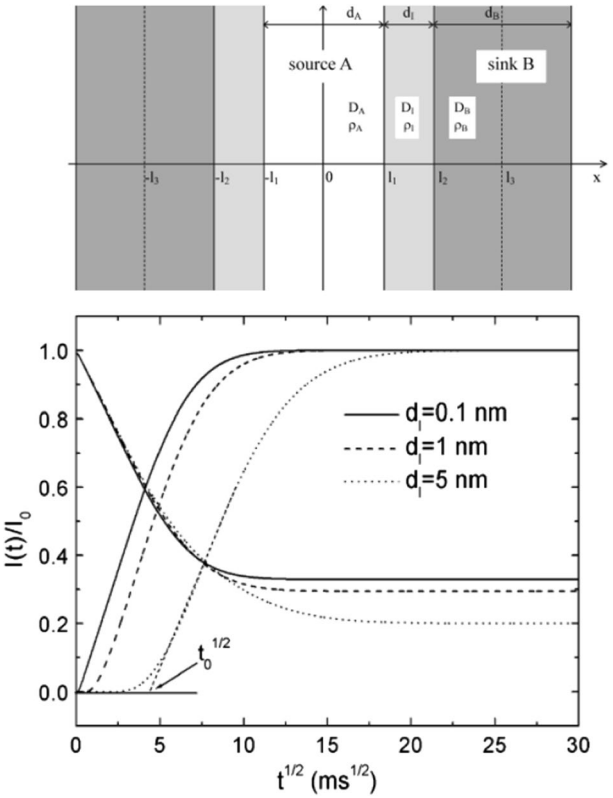

Fig. 3 The effect of the interface thickness (d_I) for the lamellar morphology on simulated decay- and build-up spin-diffusion curves for rigid (source A) and soft (sink B) domains, respectively. The initial magnetization resides in rigid domains. The spin-diffusion process is considered to be one-dimensional along the axis perpendicular to the lamellar surface, as shown in the upper part of the figure. The thickness of the source (d_A), the interface (d_I), and the sink (d_B) domains is much smaller than their dimension perpendicular to the spin-diffusion direction. The intercept of the linear region of the spin-diffusion build-up curve with the time axis is denoted by $t_0^{1/2}$ [32]

a complex discontinuous "island-like" interface between rigid and soft domains were also studied by numerical simulations for different polymers [27, 51, 52].

Precise analysis of spin-diffusion curves requires knowledge of the rate of the longitudinal (T_1) relaxation. The T_1 relaxation process and the transfer of the magnetization between different phases via spin-diffusion are two independent processes. If T_1 relaxation time largely exceeds the time needed for accomplishing the spin-diffusion process, the effect of T_1 on spin-diffusion data is negligible. However, T_1 time(s) for polymers are often comparable with the time required for completing the spin-diffusion process. This is often observed for polymers with large domain sizes and in the case of experiments performed with low-field NMR equipment. The T_1 effect progressively increases with increasing spin-diffusion time. Therefore, domain size determination using the intercept

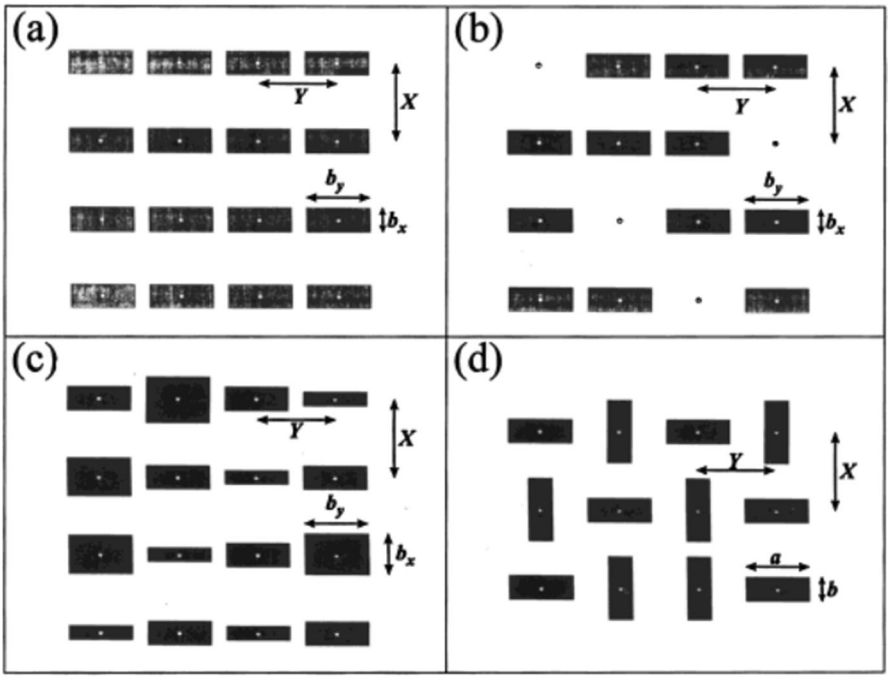

Fig. 4 Schematic 2D drawing of domain size distribution and domain clustering. Dark areas represent domains of phase I, in which the initial magnetization resides. The lattice sites are represented by the circles at the centers of phase I domains. The lattice extends to infinity in both *x*- and *y*-directions [49]. These phase geometries were used for simulations of spin-diffusion curves shown in Fig. 5

method suffers to a lesser extent from T_1-caused error than the analysis of entire spin-diffusion curves. Thus, an estimation of T_1 value for each phase is needed before performing spin-diffusion experiments. However, measured T_1 values for different phases cannot be simply related to the intrinsic rate of the T_1 relaxation in each phase. The relaxation rate depends both on the longitudinal relaxation process and on the distribution of the nuclei polarization within domains during spin-diffusion [53, 54]. If the T_1 effect cannot be ignored, two Goldman–Shen experiments with different phases of radio-frequency pulses can be used for the compensation of the T_1 effect [55]. Numerical corrections were also used to exclude the T_1 effect on spin-diffusion data. [24, 39, 43, 48, 56] The overall T_1 relaxation effect is largely eliminated by normalization of decays at different spin-diffusion times to their initial amplitude as described in publications [34, 38, 41], and shown in Figs. 1 and 8. Absorbed by polymers small molecules can also influence the shape of spin-diffusion curves if the self-diffusion rate of small molecules largely exceeds the spin-diffusion rate [57].

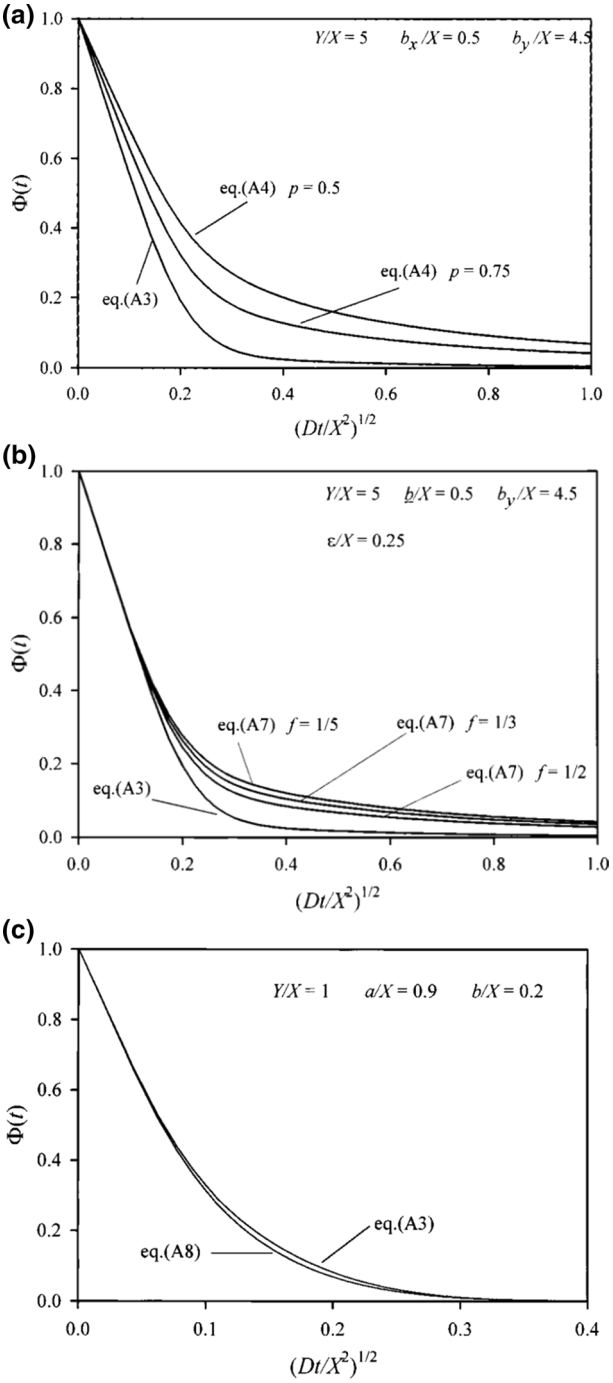

Fig. 5 The effect of domain size distribution and domain clustering on the spin-diffusion curve for the magnetization source. **a**–**c** Simulated spin-diffusion curves for morphological models b, c and d in Fig. 4, respectively. The explanation of parameters is provided in the original paper [49]

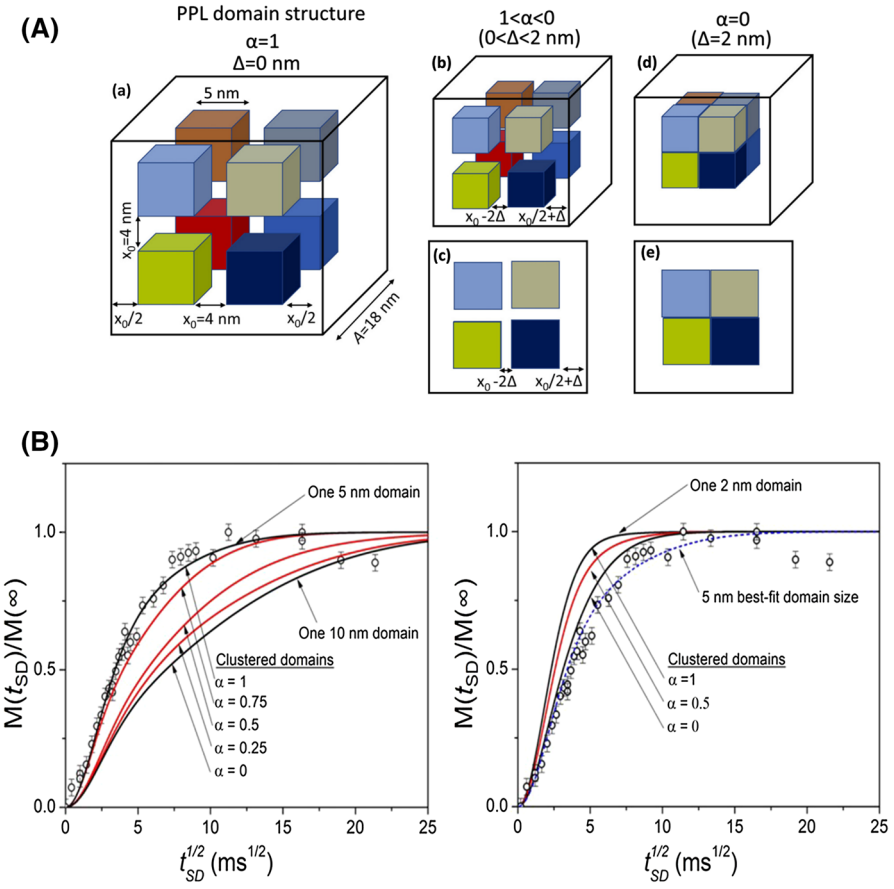

Fig. 6 Different types of clustering of domains with the fixed volume fraction of 0.21 (**A**). Clustering is characterized by α value: $\alpha=0$ represents single large domain; $\alpha=1$ corresponds to a perfect periodic domain lattice. **B** Simulated spin-diffusion curves for soft domains (the magnetization sink). Experimental data for soft domains in a polymeric membrane are shown by open circulars. The size of individual domains equals 5 and 2 nm on left and right side of **B**, respectively. The magnetization of rigid domains was selected by a DQ dipolar filter [50] (color figure online)

3 Applications of ^{1}H NMR Spin-Diffusion Method for Industrially Relevant Polymers

3.1 Polyolefins

In most ^{1}H TD-NMR studies of semicrystalline polymers, a three-phase model was used [58, 59]. The model comprises the crystalline and the amorphous phases that are separated by the crystal–amorphous interface. The same model is used for the analysis of wide-line NMR spectra [59]. If these experiments are performed at low temperatures, a significant fraction of chain segments in non-crystalline domains has low mobility and cannot be distinguished from those in polymer crystals [38, 41, 60,

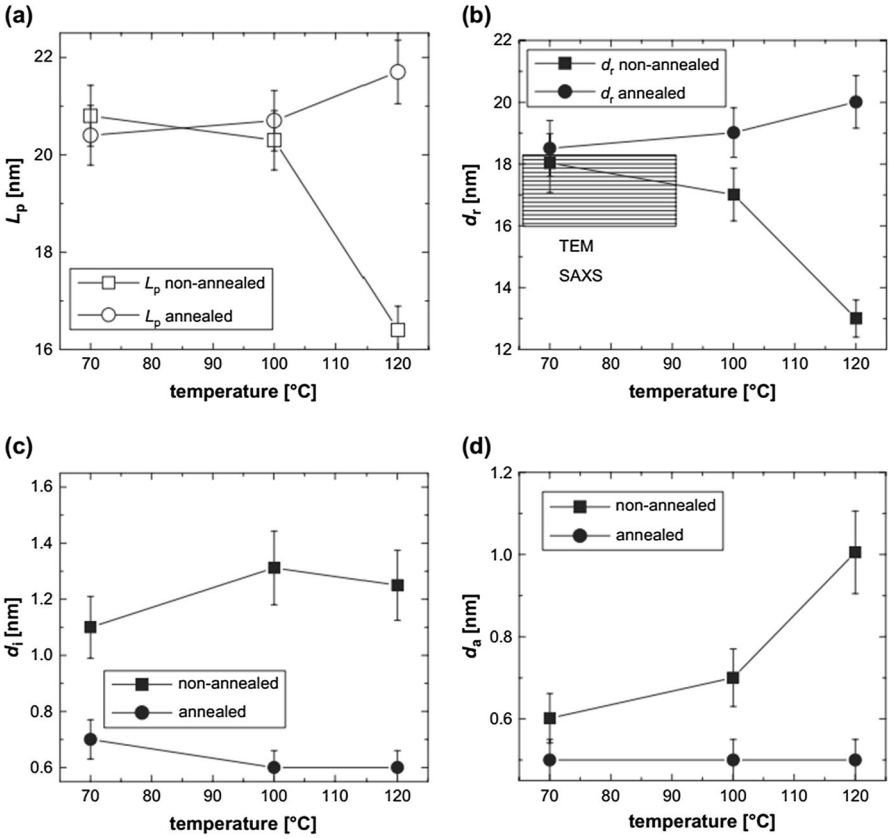

Fig. 7 The temperature dependence of the thicknesses of the periodic lamellar structures, as determined by low-field ^{1}H NMR spin-diffusion experiment for compression-molded HDPE plate that was annealed at 100 °C for 1 h. **a** Long period (L_p) that equals ($d_r + 2d_i + d_a$); **b** the lamellar thickness (d_r); **c** the thickness of semi-rigid interfacial layer separating crystalline and amorphous domains (d_i); and the thickness of soft interlamellar amorphous layers (d_a). The experiments were performed before and after 100 h annealing HDPE plates at 121 °C. The shaded area shows the lamellar thickness measured by SAXS and TEM methods for non-annealed sample [41]

61]. Therefore, the phase composition analysis should be performed at temperatures exceeding T_g of the amorphous phase by at least ~ 70–100 °C [59]. In this case, the ^{1}H NMR spin-diffusion methods can be used for determining the lamellar thickness, the thickness of the crystal–amorphous interface, and the interlamellar amorphous layers because of the sufficiently large difference in T_2 values (TD-NMR) and the full NMR line width (wide-line NMR) for these domains [38, 41, 61]. However, the temperature for the experiments should be below the melting temperature range to avoid partial melting and annealing phenomena during the data acquisition [59, 61]. High-resolution ^{13}C NMR experiments, which utilize chemical shift difference of resonances for polymer crystals and amorphous domains, are less critical to the choice of temperature for experiments [17].

The periodic lamellar structure was used for the analysis of spin-diffusion data for melt-crystallized compression-molded high-density polyethylene (HDPE) and injection-molded isotactic polypropylene (iPP) [7, 38, 41, 62]. Two types of dipolar filters were used for studying proton spin-diffusion in these polymers: the Goldman–Shen experiment [62] and a DQ dipolar filter [41]. The experiments were performed in the time-domain with a low-field NMR relaxometer and in the frequency domain by recording wide-line NMR spectra on a high-field NMR spectrometer. Wide-line NMR spectra were deconvolution into components to calculate the spin-diffusion coefficient for the crystalline and the amorphous phases, and for the crystal–amorphous interface at different temperatures (see Eqs. 3 and 4) [38, 41]. The 1D spin-diffusion model describes well all experimental data. Results for non-annealed and annealed HDPE samples are shown in Fig. 7 [41]. The studies of HDPE and iPP provided very consistent values of domain sizes in experiments with two different dipolar filters and experiments on different spectrometers. Obtained domain sizes agree well with those determined by TEM and SAXS methods. The interface thickness in melt-crystallized HDPE hardly depends on temperature and equals 1.1–1.3 nm. This value is comparable to the length of the statistical segment that consists of approximately 7 carbon–carbon bonds of PE chains. Similar interface thickness in HDPE was estimated by Monte Carlo simulations [63]. Temperature increase causes the following changes in non-annealed sample: slight increase in the interface thickness for non-annealed sample due to mobility increase of chain units at the lamellar surface; decrease in the long period and lamellar thickness in the melting temperature range due to partial melting; and nearly two times increase in the very small average thickness of interlamellar amorphous layers. These changes in non-annealed sample are caused by the preferential melting of thinner crystals and/or less thermodynamically stable crystals. Annealing of HDPE causes significant changes in domain sizes as will be discussed below. Domain thickness in injection-molded iPP sample was determined at 70, 100, and 130 °C [38]. The thickness of rigid and amorphous domains as well as the long period increase with temperature increase. These changes were explained by the melting of small disordered crystals upon increasing temperature, and by lamellae thickening. HDPE morphology was also studied using a multi-pulse selection of the proton magnetization of the amorphous phase followed by ^{13}C detection of the spin-diffusion process [37].

Morphology and domain sizes in isotactic polybutene-1 homopolymer (iPB-1) and (butene-1)-ethylene random copolymer (iPB-1/C2) were studied by spin-diffusion ^{1}H TD-NMR and SAXS experiments [34]. The typical for polyolefins' lamellar morphology is observed for iPB-1/ C2 with form I' crystals that were directly formed upon crystallization from a heterogeneous iPB-1/C2 melt (Fig. 1). A spin-diffusion experiment for iPB-1 and iPB-1/C2 with form I crystals detects different morphology, as it follows by comparing spin-diffusion curves shown in Figs. 1 and 8. Form I crystals are obtained upon polymorphic phase transition from mesomorphic form II crystals with an 11_3 helix conformation to form I polymorph with a 3_1 helix chain conformation. The phase transition causes about 20% decrease in the cross-section of the crystal unit cell, and approximately 12.6% increase in the

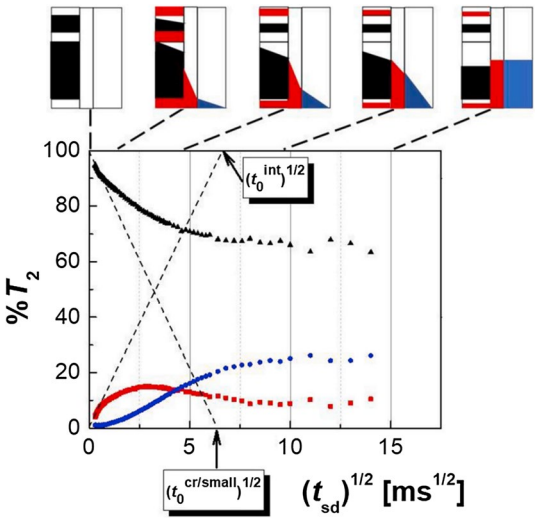

Fig. 8 Spin-diffusion build-up and decay curves for iPB-1/C2 with form I crystals that are formed during the polymorphic form II to form I phase transition. The magnetization of the crystalline phase was selected by a DQ dipolar filter. The curves for the crystalline and amorphous phases, and for two types of interfaces are shown by black triangles, blue circles, and red squares, respectively. Dashed lines are obtained by a linear regression analysis of the dependencies for the crystalline phase and the interfaces at short spin-diffusion times—$(t_{sd})^{1/2}$. Intercepts of the dashed lines with the time axis provide intercept values of $(t_o^{cr/small})^{1/2}$ and $(t_o^{int})^{1/2}$ that are used for estimation of the size of thin crystal blocks within fragmented lamellae and the inner interface shown in the schematic drawing in Fig. 9. Schematic drawing on the top shows the magnetization flow: crystalline phase → the inner interface that separates fragmented crystal blocks → the crystal–amorphous interface → amorphous phase and, finally, the equilibration of the magnetization through the sample volume [34] (color figure online)

length of the molecule within crystals [64]. One would expect that the form II to form I phase transition would affect the lamellar thickness. However, hardly any changes are observed in the crystallinity and lamellar thickness [34]. The shape of the spin-diffusion curves in Fig. 8 resembles those for significantly heterogeneous morphology, as was shown by simulations of the effect of domain size distributions and domain clustering on the spin-diffusion curves (Figs. 5 and 6). Therefore, it was suggested that the polymorphic phase transition to form I crystals causes fragmentation of crystal lamellae into small blocks with a wide size distribution (Fig. 9). Two types of interfaces are present in the polymers with form I crystals: the inner interface that separates crystal blocks within fragmented crystal lamellae, and the crystal–amorphous interface on the surface of fragmented lamellae.

3.2 Annealing Phenomena

Chain dynamics and thermodynamic factors play an important role in the annealing of semicrystalline polymers. Changes in polymer morphology during exposure of semicrystalline polymers to elevated temperatures differ for polymers with- and without chain diffusion between crystalline and amorphous

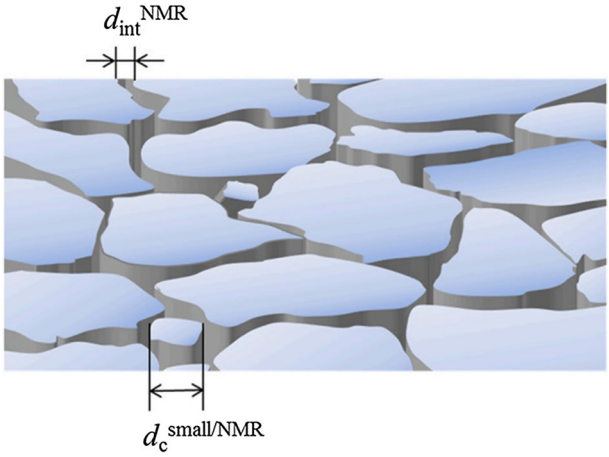

Fig. 9 Schematic drawing of a top view on the lamellar surface of iPB-1 and iPB-1/C2 with form I crystals. $d_c^{small/NMR}$ is the size of the smallest crystal blocks and d_{int}^{NMR} is the mean size of the inner interface within fragmented lamellae [34] (color figure online)

domains—crystal-mobile and crystal-fixed polymers, respectively [65]. HDPE [66], iPB [67], and iPB-1 with form II crystals [68] belong to the first class of polymers; polyamides, polyesters, and iPB-1 with form I crystals—to the second one. The difference in intra-crystalline chain dynamics influences the development of the semicrystalline morphology during crystallization [69], and its changes during annealing. ^{1}H TD-NMR and real-time synchrotron X-ray studies identified three processes with different changes in morphology upon approaching the final melting of HDPE: lamellar thickening at lower temperatures, partial melting followed by recrystallization, and progressive melting at temperatures close to the end of the melting [70]. These phenomena explain changes in domain sizes upon annealing of HDPE (Fig. 7) [41] and iPP (Figs. 10 and 11) [38]. For the both polymers, the annealing at temperatures below melting onset temperature causes an increase in the lamellar thickness at the expense of the interfacial layer and the amorphous domains without significant change in the long period (L_p). The increase in the lamellar thickness during annealing is confirmed by the increase in the crystallinity. Lamellar thickness, which was obtained by the NMR spin-diffusion method, is in good agreement with the value obtained by SAXS for the same samples (Fig. 7b). Annealing of HDPE and iPP in the melting temperature range causes an increase in the L_p and the thickness of lamellae, and a decrease in the thickness of interface and interlamellar amorphous layers (Fig. 7). These changes are caused by partial melting followed by recrystallization. The effect of annealing time and temperature on the thicknesses of crystal lamellae in iPP is shown in Fig. 11. A linear relationship of the lamellar thickness against the logarithm of the annealing time holds for all cases and agrees well with theoretical predictions and experimental results for other polymers [71]. ^{1}H TD-NMR method provides extra information on annealing-induced changes in morphology and physical phases. In addition to domain sizes, the method characterizes the crystal–amorphous interface and determines the effect of temperature and

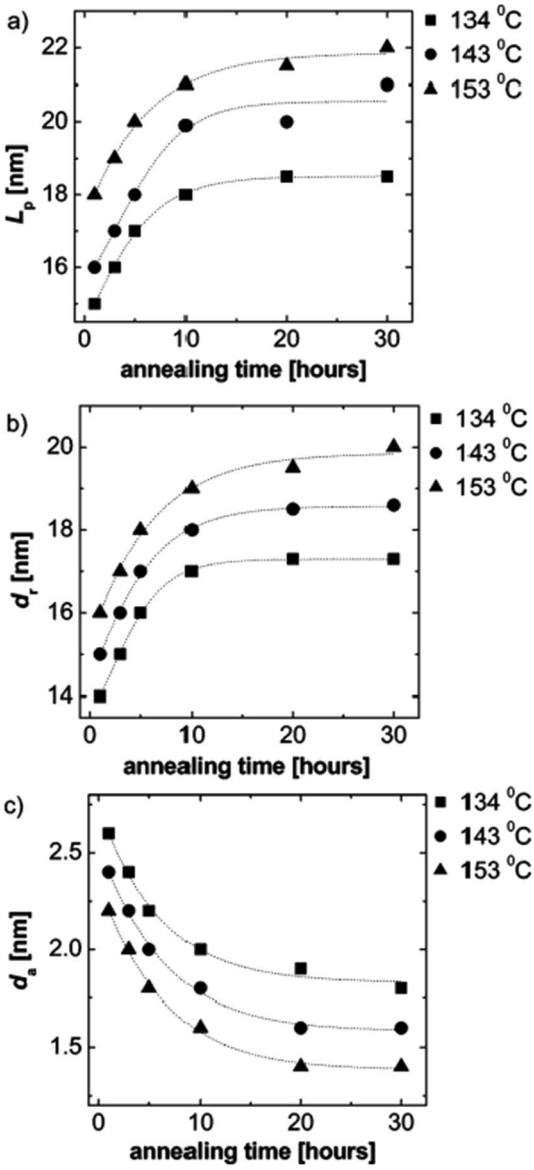

Fig. 10 Changes of the long period L_p (**a**), the thickness of crystalline (rigid) domains d_r (**b**), and amorphous (soft) domain d_a (**c**) in iPP as a function of annealing temperature and time. The domain thicknesses are determined with a low-field NMR relaxometer using spin-diffusion experiments with a DQ dipolar filter [38]

annealing time on molecular mobility in the crystalline phase, crystal–amorphous interface, and the amorphous phase.

Annealing studies of crystal-mobile polymers suggest the following mechanism of annealing-induced changes in morphology. Temperature increase causes faster chain diffusion through polymer crystals (α_{cr}-relaxation) [66, 67], and higher segmental mobility in the amorphous phase. Since lamellar thickening requires translational motion of polymer chains, both factors facilitate the structural reorganization

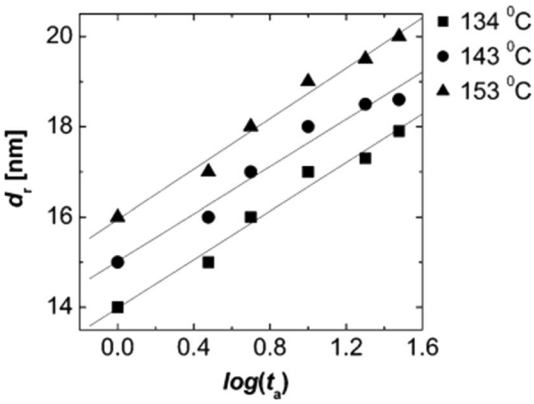

Fig. 11 Change of the thickness of crystalline (rigid) domains d_r with the logarithm of annealing time (t_a) for iPP at three different annealing temperatures [38]. The straight lines are obtained by a least-squares fit of the data using a model based on irreversible thermodynamics [71]

toward more thermodynamically stable, better-ordered crystalline structures and thicker lamellae. If annealing temperature is below the melting onset temperature, no change in the L_p is observed and the lamellar thickness increases at the expense of interlamellar amorphous layers (Figs. 7b). However, above melting onset temperature, small crystals and fewer ordered fragments of the lamellae start to melt. This process is followed by recrystallization with the formation of thicker lamellae and larger L_p (Figs. 7a, 10a). The rate of this morphology reorganization can be affected by molecular weight, since longer chains connect a larger number of lamellar crystals, which restrict the long spatial scale chain dynamic to a larger extent.

The thermal aging of crystal-fixed polymer—polyamide 4,6—was investigated by differential scanning calorimetry (DSC), SEM, WAXD, and ^{1}H NMR methods. The phase composition, chain mobility, morphology, and domain sizes were determined for injection-molded PA46 plates aged at 200 °C in an N_2-atmosphere [72]. Crystallinity increases at the expense of the crystal–amorphous interface suggesting a transformation of the interfacial layer on the lamellar surface to lamellar crystals, i.e., lamellar thickening. Chain mobility in the crystalline phase, as determined by the T_2 relaxation experiments, decreases upon aging due to molecular rearrangements causing perfection of the crystalline order. This is confirmed by WAXD analysis showing a narrowing of diffraction peaks with aging time. DSC analysis of the samples shows that less perfect crystalline structures, which are formed upon injection molding, transform into better-ordered crystals. However, 1000 h aging causes a distortion of crystalline order, as concluded from a slight decrease in melting peak temperature. This was explained by degradation processes upon long-time aging. The aging of poly(ethylene terephthalate) (PET) fibers will be discussed below.

3.3 Fibers

The most common process for producing synthetic fibers is melt spinning followed by drawing. Morphology, the phase composition, and molecular mobility of melt-spun Nylon 6 fibers were studied by ^{1}H T-D NMR T_2 relaxometry [61] and spin-diffusion experiments [28, 32]. Hydrogen atoms of water absorbed by

fibers contribute to ^{1}H NMR data. Absorbed water affects molecular mobility[61], and can influence the rate of spin-diffusion [57]. Therefore, all experiments were performed for dried fibers or those saturated with D_2O. The winding speed and the draw ratio are two important process parameters that were varied to obtain samples with widely different structural characteristics and fiber properties. The winding speed of fibers ranged from 500 to 5800 m/min, and the draw ratio was increased from 1 (undrawn fibers) to the maximum draw ratio of 4.8. The increase of these processing parameters causes a crystallinity increase from approximately 50–60 wt%, a decrease in the amount of mobile amorphous fraction and molecular mobility in this fraction [61]. A three-phase morphological model was used for the analysis of spin-diffusion curves (Fig. 12). In this model, the fibers are composed of fibrillar bundles with fibrils separated by a less-mobile amorphous layer within the bundles. Each fibril in bundles is formed by alternating crystalline and less-mobile amorphous domains. The mobile amorphous domains separate fibrillar bundles. Two spin-diffusion experiments were used: one with the MAPE dipolar filter that selects the magnetization of mobile amorphous domains [32]; and the other—with a DQ dipolar filter for the excitation of crystalline domains [28]. A 3D analytical solution of the spin-diffusion equations was used for the analysis of the spin-diffusion data. It was shown that the diameter of fibrils slightly decreases upon drawing. The bundle size increases by about 30% with increasing winding speed from 500 to 5000 m/min due to a transformation of mobile amorphous domains to crystalline and less-mobile amorphous domains within bundles. The estimated average number of fibrils in bundles ranges from 4 to 8. The diameter of the fibrils slightly decreases upon drawing.

The effect of annealing of PET fibers on the phase composition and morphology was studied with a multiple-pulse (MREV-8) ^{1}H NMR sequence that creates a magnetization gradient by utilizing the difference in the relaxation rate in fiber domains with different molecular mobility [73]. Data analysis has shown that the two-phase (crystalline-amorphous) model provides a poor representation of PET fiber morphology. Spin-diffusion equations were solved numerically for different types of three-domain morphology composed of the crystalline phase and the amorphous phase with semi-rigid and soft domains. The data analysis has indicated that these three types of domains are connected with each other. Further details concerning the spatial arrangement of the domains cannot be extracted from the modeling. The long period and crystallinity monotonically increase with increasing annealing temperatures and annealing time. The amount of semi-rigid and soft amorphous domains decreases similarly during annealing. The thinnest size of crystallites ranges from roughly 3 nm in as-drawn fiber to 7 nm in the samples annealed above 200 °C. The small size of crystallites in as-drawn fiber may cause difficulty in the detection and quantitation of crystallinity by X-ray methods. The annealing also increases the rigidity of chains in the crystallites, as concluded from ^{1}H NMR T_1 relaxation time study. If fibers are annealed without a restraint, chain orientation deteriorates strongly, which largely explains the reduced modulus and creep resistance observed in mechanical testing.

High-modulus, high-strength structures are produced by gel-spin technology from ultra-high-molecular-weight polyethylene (UHMWPE) [74]. Four different ^{1}H

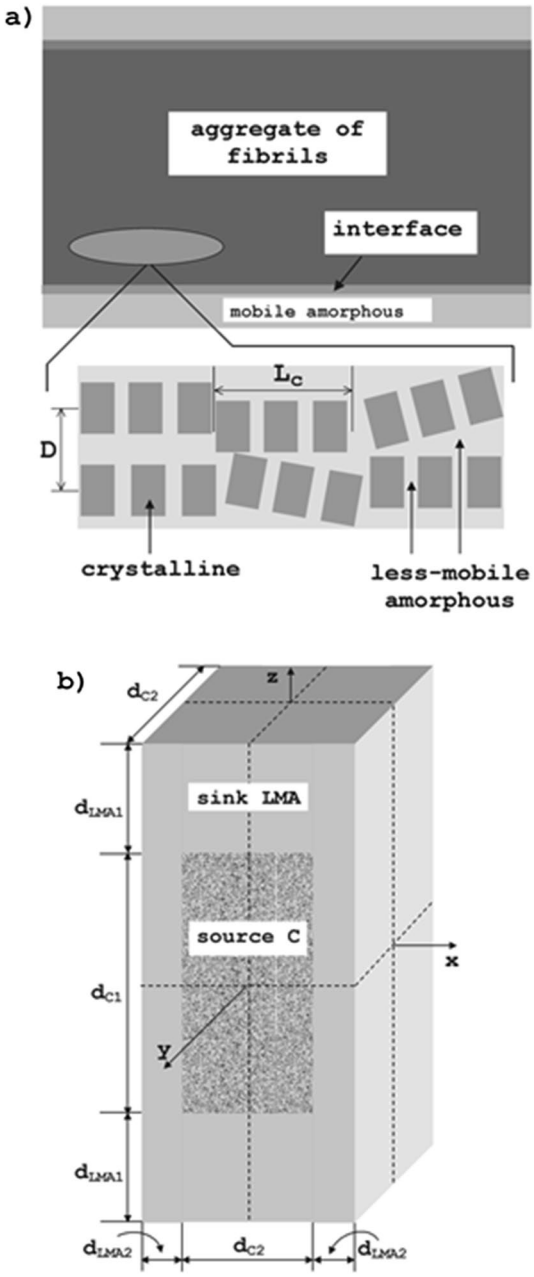

Fig. 12. **a** The model of the average Nylon-6 fiber morphology was used for interpreting the spin-diffusion experiments with the source of the longitudinal magnetization in the mobile amorphous fraction [32]. Upper part shows an aggregate of fibrils according to SAXS experiments. The distance between the fibrils is *D*. The fibrils are separated within fibrillar bundles by less-mobile amorphous domains. The axes of the fibrils is oriented approximately parallel to the fiber axis. Lamellar stacks of crystalline and less-mobile amorphous domains are well-organized along the fibrils within a coherence length L_c. **b** Schematic representation of the morphology of Nylon-6 fibers used for modeling the spin-diffusion process with the source of the longitudinal magnetization in the crystalline phase [28]. The flow of magnetization from the crystalline domain (C) into the less-mobile amorphous domains (LMA) is considered to be a three-dimensional process that takes place in a rectangular morphology. The source and sink domains have dimensions d_{C1} and d_{LMA1} along the fiber direction, and d_{C2} and d_{LMA2} in the direction perpendicular to the fiber axis

and ^{13}C NMR experiments were used for studying the phase composition, molecular mobility, and morphology of one gel-spun UHMWPE fiber [75]. Five morphological fiber components were identified: 83% crystal core with 80% of orthorhombic and 3% of monoclinic crystals and core thickness of ~ 100 nm; 5% disordered

all-*trans* interface and/or tie molecules; 11% mobile amorphous regions with diameter of ~ 10 nm; and 1% highly mobile segments that probably locate at void surfaces. Rigid gauche conformers could not be detected at a concentration above 1%. The presence of microvoids in gel-spun UHMWPE fibers was shown by ^{129}Xe NMR spectroscopy [76]. This NMR method measures voids with diameters larger than 0.44 nm. The mean volume of microvoids increases as a function of applied strain at a final drawing of UHMWPE fibers.

Physical structures, morphology, and final fiber properties largely depend on the processing conditions. The effect of draw ratio on physical phases and morphology was studied for a series of gel-spun UHMWPE fibers by ^{1}H wide-line NMR spin-diffusion experiments, ^{1}H T_2 relaxation experiments, WAXD, and SAXS methods [77]. The crystallinity of fibers, as determined by WAXD and T_2 relaxation methods, increases from approximately 89 to 96 wt% with increasing draw ratio at the expense of amorphous domains with largely restricted chain mobility. Approximately 1 wt% of highly mobile chain segments ($T_2 \approx$ 1–1.5 ms) were detected in all fibers by the Hahn-echo T_2 relaxation experiment. Such long T_2 value is observed for UHMWPE melts [78], which suggests that highly mobile segments locate at void surfaces [76]. WAXD, SAXS, and NMR spin-diffusion methods offered different contrast to semicrystalline morphology (Fig. 13). WAXD and SAXS methods discriminate between crystalline and amorphous domains based on differences in the electron density and periodicity of these domains at different length scales, namely WAXD—at the crystal lattice level, and SAXS—at larger length scale of semicrystalline superstructure level. The NMR method utilizes differences in chain mobility in fiber domains. Therefore, the X-ray and NMR methods provide complementary information about fiber morphology. The average crystal size in the direction perpendicular to the fiber axis [d_c(WAXS)] was determined by WAXD. The long period (L) and the stem

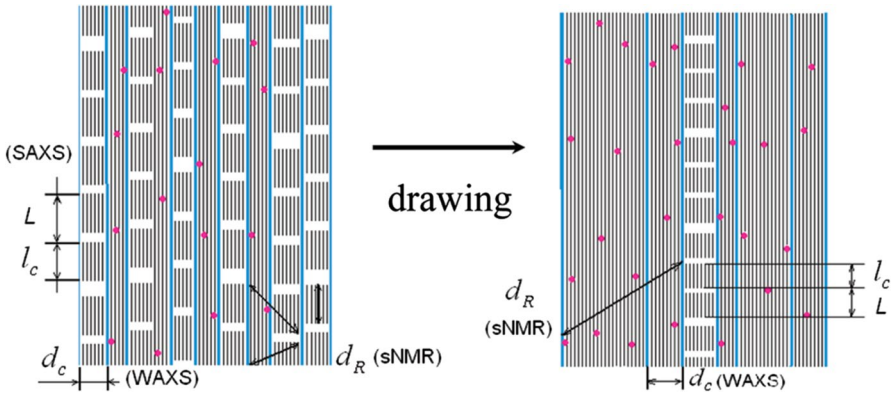

Fig. 13 Schematic 2D drawing of the morphological features of gel-spun UHMWPE fibers prepared using two draw ratios. The model shows the main morphological elements that are present in fibers and not their dimensions. The thick blue lines show boundaries of the fibrils or large crystals with loss of the crystal structure coherency across the lines. The large white areas correspond to amorphous domains and the small red dots—to voids and defects in large crystals. The designation of crystal dimensions, as measured by different methods, is shown in this figure and explained in the text [77] (color figure online)

length of crystalline blocks in fibrils (l_c) were obtained by SAXS. NMR spin-diffusion experiments determined weight-average shortest-distance-across rigid domains [d_R(sNMR)]. The results acquired by these methods suggest that the fiber morphology can be described by a mixture of fibrils with the long period of ~35–45 nm, as determined by WAXD, and large so-called chain-extended crystals that are detected by SAXS. The size of rigid domains in ultimately drawn largely exceeds the dimension of crystal blocks in fibrils as determined by the X-ray methods. The difference was explained as follows. The NMR method provides the total thickness of rigid domains that are composed of two or more crystalline domains with adjacent either intra- and/or interfibrillar rigid amorphous layers with low chain mobility, while SAXS—the long period (L) and the stem length of crystalline blocks in fibrils (l_c), and WAXD—the average crystal size [d_c(WAXD)] in the direction perpendicular to the fiber axis.

3.4 Filled Rubbers

The mechanical properties of rubbers are strongly improved by their reinforcing with active fillers. The most frequently used filler in the rubber industry is carbon black. A number of factors contribute to the significant improvement of rubber properties after the incorporation of active fillers. Among the most important factors determining the rubber reinforcement, the following should be mentioned: strain amplification due to the filler volume effect, filler–filler networking, and filler–rubber interactions [79]. Molecular mobility of chain segments at the carbon black surface—rubber–filler interface or adsorption layer—is largely restricted by adsorption interactions, as was shown by ^{1}H T_2 relaxation experiments for carbon black filled ethylene-propylene-diene rubbers (EPDM) [80, 81]. In addition to the rubber–filler interface, two other types of chain segments with different anisotropy of segmental motions are present in filled rubbers (Fig. 14). (1) Chains with restricted

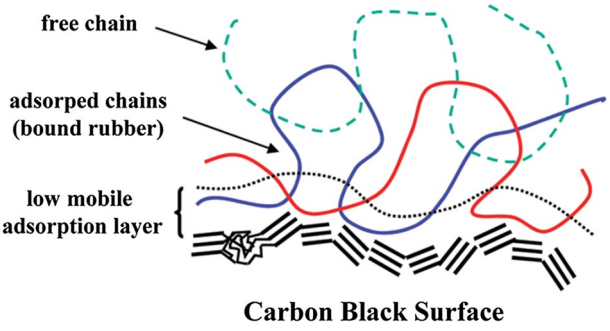

Fig. 14 Simplified, graphical representation of EPDM chains adjacent to the carbon black surface. Parallel short lines show graphite layers of carbon black nanocrystals. Solid and dashed lines show fewer mobile chains adsorbed at the carbon black surface and more mobile chains without contact with carbon black, respectively. The dotted line indicates the interfacial layer. The low-mobile chain segments at the filler surface provide adsorption network junctions for the rubber matrix, explaining the origin of bound rubber. Free rubber chains in the bulk rubber have hardly any contact with the surface of the carbon black and can be removed from unvulcanised mixtures by extraction with a good solvent [79] (color figure online)

large-spatial-scale segmental mobility that have multiple adsorption junctions at the carbon black surface. These chains form the so-called bound rubber that cannot be extracted from the mixture even in a good solvent [81]. (2) Free or extractable rubbery chains with a relatively low number of adsorption junctions or without direct contact with carbon black surface [79, 81]. Similar structures were observed in silica-filled natural rubber [82] and polydimethylsiloxane [83, 84].

The characterization of the rubber-filler interface by the T_2 relaxation method is complicated by two effects: the presence of free radicals on the surface of carbon black [85]; and the magnetic field gradients introduced by the filler due to magnetic-susceptibility differences between filler particles and the rubber matrix [86], and other solid-soft matters [87]. Therefore, to prove the existence of low-mobile chain segments at the surface of carbon black, the spin-diffusion experiment with a DQ dipolar filter was performed for unfilled and carbon black filled EPDM rubber [79]. The initial amplitude of a signal decay, which was recorded in the transverse direction in the DQ experiment, was compared at different excitation times (t_{ex}) for non-cross-linked EPDM without carbon black and for the bound rubber sample (Fig. 15). The intensive maximum is observed at approximately 500 and 300 μs for the unfilled and carbon black bound EPDM, respectively. It was shown that the maximum on DQ curves for rubbers shifts to lower t_{ex} with increasing network density that is formed either by chemical cross-links and/or physical junctions [33]. Thus, chain adsorption in the bound rubber causes the formation of physical network junctions. A shallow maximum at ~ 25 μs directly proves the immobilization of EPDM chain segments at the carbon black surface. Additional information was obtained by spin-diffusion experiments. Figure 16 shows FIDs that were recorded at four different spin-diffusion times (t_{sd}). In this experiment, the magnetization of the immobilized chain segments was selected with a DQ dipolar filter. At short t_{sd}, the fast decaying component, which originates from the immobilized chain units, is mainly observed. Upon increasing t_{sd} from 0.49 to 50 ms, the intensity of this component decreases,

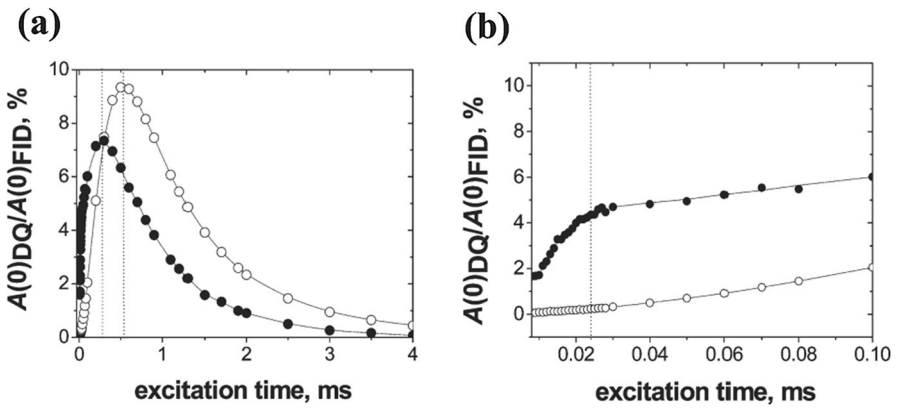

Fig. 15 **a** The initial amplitude of the signal decay, which was recorded in the transverse direction in a DQ experiment, against the excitation time (t_{ex}) for the bound rubber sample (closed circles) and the nonvulcanized EPDM without carbon black (open circles). **b** Expansion of the dependence at short excitation times [79]

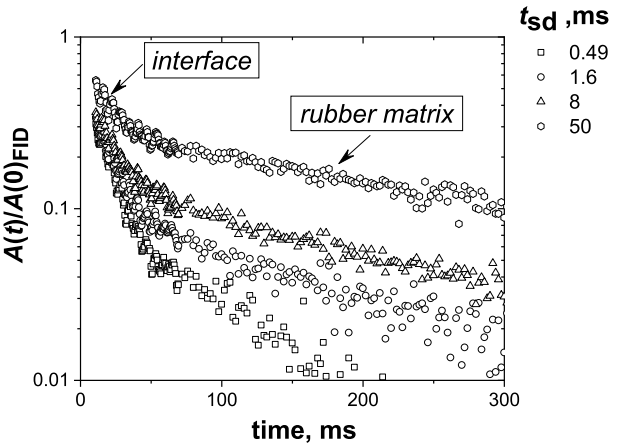

Fig. 16 The FID at different mixing times (t_{sd}) in the spin-diffusion experiment performed for the bound rubber sample. The magnetization of low-mobile adsorbed chain segments was selected by a DQ dipolar filter. Each decay is normalized to its initial amplitude [79]

whereas the intensity of the component with a long decay time, which is associated with the mobile rubbery matrix, increases. This behavior is typical for heterogeneous polymers that are composed of rigid and soft domains. These results confirm the existence of an immobilized rubber layer covering the surface of the carbon black. The presence of the immobilized layer was recently observed in a spin-diffusion study of silica-filled poly(ethyl acrylate) [52]. It was proposed that domains with low chain mobility may either form a separate shell-like layer or nanometer-sized subdomains.

3.5 Ionomers

Polymers with a small amount of ion-containing monomer units (up to about 15 mol %) represent a separate class of materials that are of great interest for both fundamental research and industrial applications. One type of these polymers are telechelic ionomers that have strongly attracting ionic groups at the chain ends. One example of telechelic ionomers is an unsaturated polyester (UP) that is dissolved in styrene and mixed with a small amount of MgO [36]. The reaction of the metal oxide with the carboxylic end groups of UP leads to a 10^3–10^4-fold viscosity increase during storage of the initial solution with MgO. The rate of thickening and the resulting viscosity determine the processability of the material.

The molecular mechanisms of the thickening of UP styrene solutions with MgO were studied by ^{1}H and ^{13}C NMR, SAXS, and WAXD methods [36]. ^{1}H NMR T_2 relaxation decay of the initial UP solution consists of two components with characteristic decay times of 2.3 and 29 ms—T_2^{in} and T_2^l, respectively. These relaxation components largely originate from the relaxation of less-mobile UP chain segments—T_2^{in} relaxation component, and more mobile UP chain end segments and styrene molecules—T_2^l relaxation component. A third relaxation component with

short decay time T_2^s is detected shortly after the solution was mixed with MgO. The value of T_2^s is typical for glassy-like polymers. ^{13}C NMR spectra reveal that only a very small fraction of the styrene molecules show significantly reduced mobility, indicating that almost no styrene molecules are trapped in the immobilized domains. Thus, the fraction of T_2^s relaxation component represents the proton fraction of largely immobilized UP chain segments with respect to the total proton content in UP. The relative fraction of immobilized UP chain segments ($\%T_2^s$) increases with thickening time at the expense of the most mobile UP chain end segments ($\%T_2^{in}$) and styrene molecules ($\%T_2^l$), as shown in Fig. 17. Approximately one-third of UP resin chain units becomes immobilized during 1500 h storage of UP solution mixed with MgO. About half of the styrene molecules locates in zones with significantly reduced chain mobility (T_2^{in} relaxation) outside domains with immobilized UP chain segments. The mobility of these styrene molecules is strongly coupled to that of UP chains. WAXD experiment of the thickened compound detects the presence of crystals. Crystalline reflections are not sharp because of small crystal size in at least one dimension. Thus, the data exclude the presence of three-dimensional spherical or cylindrical shapes of immobilized domains. SAXS experiments reveal a superlattice that is formed by lamellae with the lattice periodicity varying from 2 to 12 nm and with a preferred lamellar spacing of 3 nm. The last value is comparable to the mean end-to-end distance of UP chains. The initial slope of the spin-diffusion curve for domains with immobilized chain units hardly changes with thickening time (Fig. 18), whereas the amount of these domains ($\%T_2^s$) continuously grows with time (Fig. 17). This should be the case of growing lamellae with approximately the same thickness. The lamellar thickness, as estimated by NMR spin-diffusion experiment, equals approximately 6 nm. This value is larger than the value estimated by

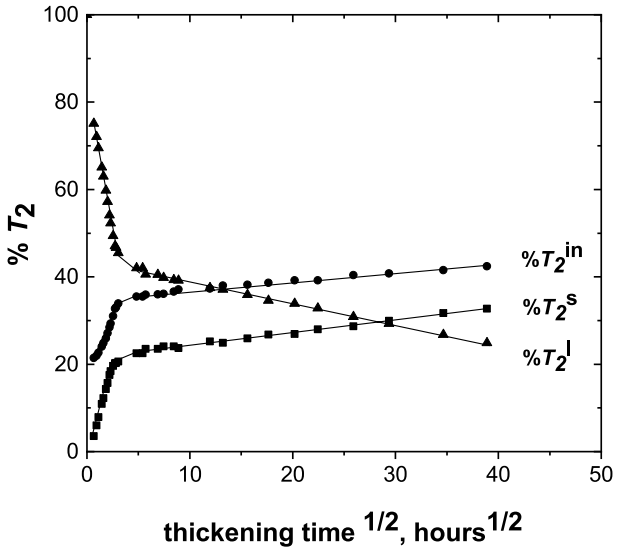

Fig. 17 Relative fraction of the relaxation components in UP styrene solution mixed with MgO against the square root of the thickening time. The lines are guides to the eye [36]

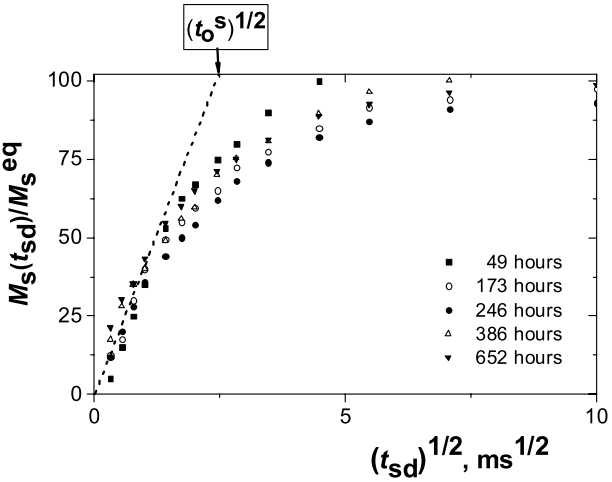

Fig. 18 Results of the Goldman–Shen spin-diffusion experiment for UP styrene solution mixed with MgO. The different symbols correspond to different storage times of UP-MgO resin solution, as shown in this figure. The data points show the growth of the magnetization of immobilized domains with increasing mixing time t_{sd} in the experiment. The transverse magnetization of the immobilized chain segments $M_s(t_{sd})$ at different mixing times is normalized to its equilibrium value M_s^{eq}. The dotted line shows the initial slope of the spin-diffusion curve that does not change with resin storage time [36]. Its extrapolation to the *x*-axis provides an intercept value $(t_0^s)^{1/2}$, which is used for the estimation of the thickness of lamellae

SAXS, because SAXS method detects the inner part of the lamellae with high electron density, i.e., the carboxylate-Mg^{2+} ions core of the lamellae, whereas the ^{1}H NMR method distinguishes lamellae based on low-mobile protons on chain segments of the UP resin. The following main mechanism, which is involved in the viscosity increase, was established. Strong electrostatic interactions between Mg^{2+} ions and the charged carboxylate chain ends cause the formation of crystalline carboxylate–Mg^{2+}–aqua complexes in the crystalline core part of the lamellae that is detected by WAXD (Fig. 19b). The core part is surrounded by a glassy-like layer of UP chain segments that stick out of the lamellar plane. This layer is characterized by the T_2^s relaxation process. UP chains interconnect neighboring lamellae, as shown in the schematic drawing of the morphology of thickened UP (Fig. 19a). On the basis of the thickening mechanism, the influence of different factors on the thickening of polyesters with metal oxide was established.

The thermo-reversible nature of the ionic associations in ionomers with a low T_g can make possible recycling of these viscoelastic materials. Low T_g ionomers behaves like cross-linked elastomers at a service temperature, but they can be melt-processable at elevated temperatures due to a weakening of ionic interactions resulting in a viscosity decrease. Ethylene–propylene copolymer (EPM) with randomly grafted maleic anhydride (MAn)—(MAn-*g*-EPM)—belongs to this class of viscoelastic materials. The morphology of a series of samples with different degrees of neutralization (DN) by zinc acetate was studied by SAXS and ^{1}H NMR spin-diffusion methods [88]. Both methods detect the formation of

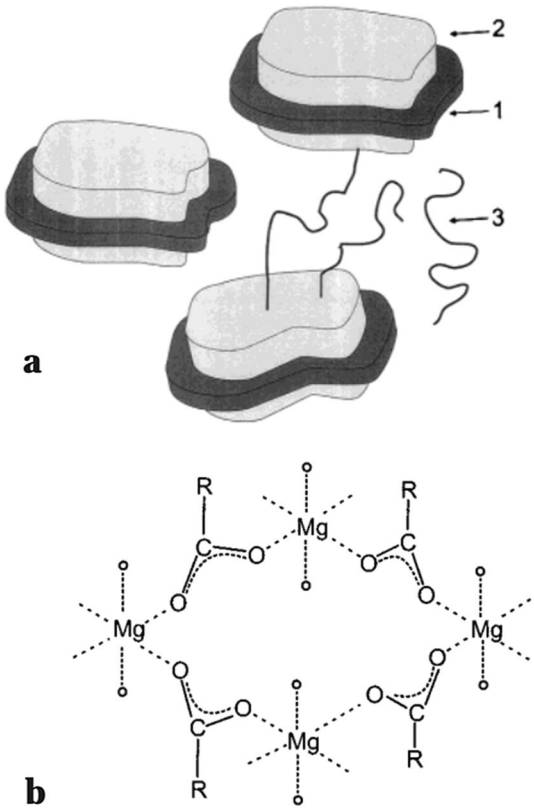

Fig. 19 **a** Schematic drawing of the morphology of thickened UP styrene solution mixed with MgO: (1) ion-containing core; (2) immobilized UP chain segments covering the carboxylate-Mg^{2+} ions core of the lamellae; (3) domains with UP network chains, dangling chains, free chains, and styrene molecules. **b** Hypothetical structure of the crystalline core of the lamellae, where open small circles represent water molecules. In this figure, just one-fourth of the unit cell is given, corresponding to the asymmetric unit [36]

immobilized aggregates that are composed of polar groups, zinc ions, and EPM chain fragments. The aggregates act as multi-functional network junctions. The type of spin-diffusion curves is typical for heterogeneous materials with interfaces (Fig. 20). Three types of EPM chain units with different mobility were detected by ^{1}H T_2 relaxometry in the ionomer precursor (DN = 0) and in samples with different DN: (1) low-mobile chain segments in the aggregates that contain grafted MAn chain units and its salts with Zn^{2+}; (2) chain segments with intermediate mobility in the interfacial layer surrounding the aggregates; and (3) the viscoelastic matrix that contain EPM unentangled and entangled network chains interconnecting these aggregates and more mobile network defects, such as dangling chain ends and chain loops. According to the SAXS and NMR spin-diffusion analysis, the morphology can be described by ionic spherical aggregates with high electron density that are surrounded by an interfacial EPM layer with restricted chain mobility (Fig. 21). The radius of the aggregates is about 1.5–2 nm and the thickness of the interface is about 1–1.5 nm. The aggregates are embedded in the viscoelastic EPM matrix. NMR T_2 relaxometry shows that the density of the ionic network junctions and the strength of the ionic aggregates increases

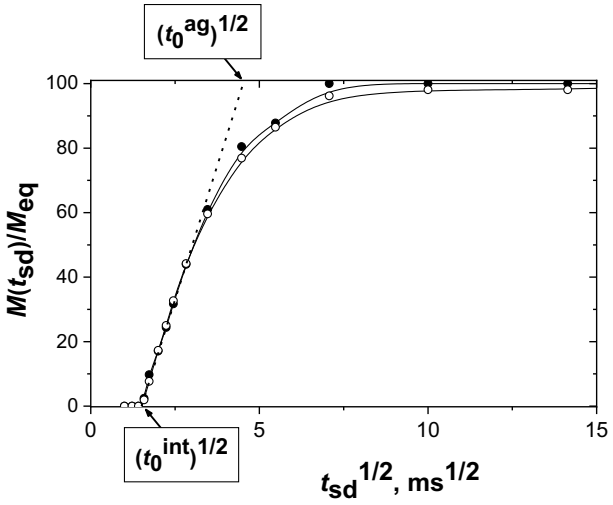

Fig. 20 The growth of the transverse magnetization of the immobilized polymer chain segments $[M(t_{sd})/M_{eq}]$ to its equilibrium value, as recorded by the Goldman–Shen spin-diffusion experiment for MAn-*g*-EPM with two different degrees of neutralization (DN) with zinc acetate. The data for samples with DN of 10% and 100% are shown by solid and open circles, respectively. The dotted line shows the slope of the spin-diffusion curves in the initial spin-diffusion time regime. Its extrapolation to the *x*-axis provides intercept values $(t_0^{int})^{1/2}$ and $(t_0^{ag})^{1/2}$, which are used for the estimation of the interface thickness and the size of aggregates [88]

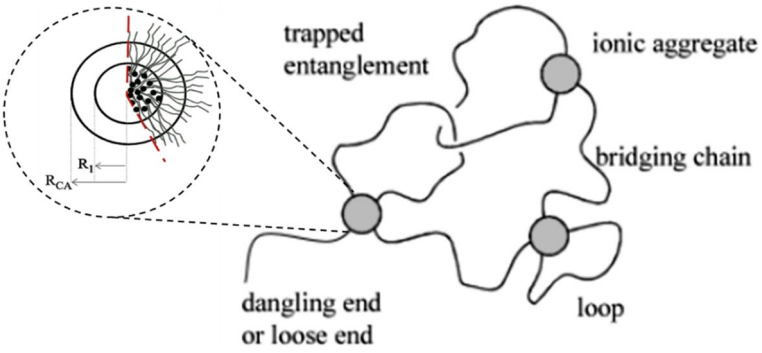

Fig. 21 Schematic representation of the ionomeric network with ionic aggregates that acts as multi-functional network junctions. Lines show the network of physical junctions that is formed by bridging chains, entangled chains, chain loops, and dangling chain ends. A schematic representation of an aggregate in Man-*g*-EPM-based ionomers and its precursor is shown on the insert. Black circles represent grafted onto EPM chains MAn units either neutralized with zinc acetate or un-neutralized [88] (color figure online)

with DN increase. These changes lead to the improvement of several macroscopic properties of this material, such as compression set and tensile properties.

3.6 Thermoplastic Polyurethanes

Thermoplastic polyurethanes (TPUs) belong to the other important class of elastomers. They combine the processability of thermoplastics with good mechanical performance. In most cases, segmented TPUs are multiblock linear copolymers with alternating hard (HS) and soft (SS) segments. Phase-separated microstructures, which are formed by hard segments, serve as reinforcing fillers and act as multi-functional physical cross-links to the soft domains. The morphology and domain sizes were studied for a series of TPUs with different content of HS, which was varied was from 23 to 54 wt%, and SS with the same molecular weight [46]. The TPU phase structure can be well described by hard and soft phases with the mixed HS-SS phase incorporated in the soft domains, as was shown by an analysis of ^{1}H wide-line NMR spectra. Spin-diffusion experiments with a ^{1}H DQ dipolar filter were used to establish the dominant dimensionality of HS domains and their effective dimensions. At the higher HS amount, proton spin diffusivities increase both in HS and SS domains due to better packing effects and larger hindrances of segmental motions. 1D, 2D, and 3D solutions of the spin-diffusion equations were used for the analysis of experimental spin-diffusion curves (Fig. 2). In these simulations, the hard domains were considered to be embedded in the soft SS matrix. The morphology can be inverted for other than in the study molar mas of SS and HS contents. The 3D spin-diffusion model describes well the dimensionality of HS domains. The effective size of these domains increases linearly from approximately 7 to 14 nm with the increase in the HS amount from 23 to 54 wt%. This change is accompanied by a decrease in the effective size of soft domains from 8 to 5 nm.

4 Conclusions

The review presents applications of ^{1}H time-domain NMR spin-diffusion methods for quantitative analysis of domain sizes and dynamic heterogeneities for several polymeric materials of industrial interest. Domain sizes obtained by NMR are in good agreement with the results of SAXS, WAXD, and TEM methods for the same materials. The NMR spin-diffusion method could be advantageous to traditional methods for studying the morphology in some of materials, since the method exploits the contrast in molecular mobility in different phases in multiphase organic materials. Given examples demonstrate the strength of the method for studying morphology of complex polymeric materials. In addition to the types of morphological structures and domain sizes, the NMR method determines the dynamic heterogeneity of materials, interfacial layers at the border of different phases, the structure of the physical network interconnecting domains in heterogeneous polymers, and molecular mobility in different phases. Thus, combined analysis of the results of different methods provides in-depth information for a better understanding of structural heterogeneities in polymers and their effect on macroscopic properties.

Acknowledgements VL acknowledges long-standing research collaboration with Prof. B. Blümich, Prof. D. E. Demco, and members of their groups.

Author Contributions VL generated the main idea of the review and wrote most of the text. Several topics in the review were discussed with YM. YM acquired funding and arranged project administration. Both authors reviewed the manuscript and approved it for the publication.

Funding This work was supported by the National Natural Science Foundation of China (Grant No. 22161132007).

Availability of Data and Materials The review provides an overview of published studies and does not present any original unpublished data and materials. Data and materials should be requested from authors of cited papers.

Declarations

Conflict of Interest The authors have not financial or personal nature interests that are directly or indirectly related to the work.

Ethical Approval Not applicable.

References

1. Q. Guo. Polymer morphology: principles, characterization, and processing. (Wiley & Sons Ltd, 2016). (ISBN: 978-1-118-45215-8)
2. V.M. Litvinov, V.B.F. Mathot, Partitioning of main and side-chain units between different phases: a solid-state ^{13}C NMR inversion-recovery cross-polarization study on a homogeneous, metallocene-based, ethylene-1-octene copolymer. Solid State Nucl. Magn. Res. **22**, 218–234 (2002). https://doi.org/10.1006/snmr.2002.0078
3. D.R. Salem, *Structure formation in polymeric fibers* (Hanser Publishers, Munich, 2000). (**ISBN: 978-3-446-18203-5**)
4. N. Hadjichristidis, S. Pispas, G. Floudas. Block Copolymers Morphology. in: Block Copolymers: Synthetic Strategies, Physical Properties, and Applications. (John Wiley & Sons, Inc, Hoboken, NJ, 2003), pp. 346–361. https://doi.org/10.1002/0471269808.ch19
5. L.C. Sawyer, D.T. Grubb, *Polymer microscopy* (Springer, Dordrecht, 1996). (**ISBN: 978-94-015-8595-8**)
6. A.R. Clarke, C.N. Eberhardt, *Microscopy techniques for material science* (Woodhead Publishing Ltd, Cambridge, 2002). (**ISBN 978-1-85573-587-3**)
7. M.R. Libera, R.F. Egerton, Advances in the transmission electron microscopy of polymers. Polym. Rev. **50**, 321–339 (2010). https://doi.org/10.1080/15583724.2010.493256
8. B. Crista, J. M. Schultz. Atomic force microscopy studies of polymer crystals: Nucleation, growth, annealing, and melting. in: Encyclopedia of Polymers and Composites. (Springer-Verlag, Berlin, Heidelberg, 2013) pp. 1–25. https://doi.org/10.1007/978-3-642-37179-0_23-1
9. D.V. Chapman, H. Du, W.Y. Lee, U.B. Wiesner, Optical super-resolution microscopy in polymer science. Progr. Polym. Sci. **111**, 101312 (2020). https://doi.org/10.1016/j.progpolymsci.2020.101312
10. J. Alvarez, G. Saudino, V. Musteata, P. Madhavan, S.P. Nunes, G. Saudino, C. Boi, A. Genovese, A. Reza Behzad, R. Sougrat, K.-V. Peinemann, 3D analysis of ordered porous polymeric particles using complementary electron microscopy methods. Sci. Rep. **9**, 13987 (2019). https://doi.org/10.1038/s41598-019-50338-2
11. R.-J. Roe, *Methods of X-ray and neutron scattering in polymer science* (Oxford University Press, New York, 2000). (**ISBN 0-19-511321-7**)
12. N. Stribeck, X-ray scattering of soft matter. (Springer, Berlin, Heidelberg, 2007). ISBN: 978-3-540-69856-*2

13. A. Seidlitz, T. Thurn-Albrecht. (2016). Small-angle X-ray scattering for morphological analysis of semicrystalline polymers. in *Polymer Morphology: Principles, Characterization, and Processing*, ed. By Q. Guo. (John Wiley & Sons, Inc., 2016), pp. 151–164. https://doi.org/10.1002/9781118892756.ch9
14. C. A. Avila-Orta, F. J. Medellin-Rodrigue, Small-angle X-ray scattering of polymer systems. in *Polymer Morphology: Principles, Characterization, and Processing*, ed. By Q. Guo. (John Wiley & Sons, Inc., 2016), pp. 391–407. https://doi.org/10.1002/9781118480793.ch19
15. D. Balzar, N. Audebrand, M. Daymond, A. Fitch, A. Hewat, J. I. Langford, A. Le Bail, D. Louër, O. Masson, C. N. McCowan, N. C. Popa, P. W. Stephens, B. Toby. Size-strain line-broadening analysis of the ceria round-robin sample. J. Appl. Crystallography *37*, 911–924 (2004). https://tsapps.nist.gov/publication/get_pdf.cfm?pub_id=851306
16. V.J. McBrierty, K.J. Packer, *Nuclear magnetic resonance in solid polymers* (Cambridge University Press, Cambridge, 1993). (**ISBN: 9780511525278**)
17. K. Schmidt-Rohr, H.W. Spiess, *Multidimensional solid-state NMR and polymers* (Academic Press, London, 1994). (**ISBN: 9780080925622**)
18. R. A. Larsen. Raman spectroscopy of polymers. in *Applied Polymer Science: 21st Century,* ed. By C. D. Craver, C. E. Carraher, Jr. (Elsevier, 2000), pp. 759–785. https://doi.org/10.1016/B978-008043417-9/50038-6
19. J.L. Koenig, J.P. Bobiak, Raman and infrared imaging of dynamic polymer systems. Macromol. Mater. Engineering **292**, 801–816 (2007). https://doi.org/10.1002/mame.20070001
20. P. Blümler, S. Hafner. Nuclear magnetic resonance, Imaging of polymers. in *Encyclopedia of Analytical Chemistry*. ed. By R. A. Meyers. (John Wiley & Sons, Ltd., 2009). https://doi.org/10.1002/9780470027318.a2023.pub2
21. P. Adriaensens, A. Pollaris, R. Rulkens, V.M. Litvinov, J. Gelan, Study of water uptake in polyamide 46 copolymers by magnetic resonance imaging relaxometry. Polymer **45**, 2465–2473 (2004). https://doi.org/10.1016/j.polymer.2004.02.007
22. P. Adriaensens, L. Storme, R. Carleer, J. D'Haen, J. Gelan, V.M. Litvinov, R. Marissen, J. Crevecoeur, NMR imaging study of stress-induced material response in rubber modified polyamide 6. Macromolecules **35**, 135–140 (2002). https://doi.org/10.1021/ma0113273
23. S. N. Magonov. Atomic Force Microscopy in Analysis of Polymers. in *Encyclopedia of Analytical Chemistry: Applications, Theory and Instrumentation*. ed. By R. A. Meyers. (John Wiley & Sons, Ltd., 2009). https://doi.org/10.1002/9780470027318.a2003
24. J. Clauss, K. Schmidt-Rohr, H.W. Spiess, Determination of domain sizes in heterogeneous polymers by solid-state NMR. Acta Polym. **44**, 1–17 (1993). https://doi.org/10.1002/actp.1993.010440101
25. D.E. Demco, A. Johansson, J. Tegenfeldt, Proton spin diffusion for spatial heterogeneity and morphology investigations of polymers. Solid State Nucl. Magn. Res. **4**, 13–38 (1995). https://doi.org/10.1016/0926-2040(94)00036-C
26. K. Landfester, H.W. Spiess, Characterization of interphases in core–shell latexes by solid-state NMR. Acta Polym. **49**, 451–464 (1998). https://doi.org/10.1002/(SICI)1521-4044(199809)49:9%3C451::AID-APOL451%3E3.0.CO;2-U
27. H. Schneider, K. Saalwachter, M. Roos, Complex morphology of the intermediate phase in block copolymers and semicrystalline polymers as revealed by ^{1}H NMR spin diffusion experiments. Macromolecules **50**, 8598–8610 (2017). https://doi.org/10.1021/acs.macromol.7b00703
28. A. Buda, D.E. Demco, M. Bertmer, B. Blümich, V.M. Litvinov, J.P. Penning, Complex morphology of melt-spun Nylon 6 fibers investigated by ^{1}H double-quantum-filtered NMR spin-diffusion. ChemPhysChem **5**, 876–883 (2004). https://doi.org/10.1002/cphc.200301071
29. M. Munowitz, A. Pines, Principles and applications of multiple-quantum NMR. Adv. Chem. Phys. **66**, 1–152 (1986). https://doi.org/10.1002/9780470142929.ch1
30. R.R. Ernst, G. Bodenhausen, A. Wokaun, *Principles of nuclear magnetic resonance in one and two dimensions* (Clarendon Press, Oxford, 1987). (**ISBN: 9780198556473**)
31. M. Goldman, L. Shen, Spin-spin relaxation in LaF_3. Phys. Rev. **144**, 321–331 (1966). https://doi.org/10.1103/PhysRev.144.321
32. A. Buda, D.E. Demco, M. Bertmer, B. Blümich, V.M. Litvinov, J.P. Penning, General analytical description of spin-diffusion for a three-domain morphology. Application to melt-spun Nylon 6 fibers. J. Phys. Chem. B **107**, 5357–5370 (2003). https://doi.org/10.1021/jp021684v
33. V.M. Litvinov, EPDM/PP thermoplastic vulcanizates as studied by proton NMR relaxation: phase composition, molecular mobility, network structure in the rubbery phase, and network heterogeneity. Macromolecules **39**, 8727–8741 (2006). https://doi.org/10.1021/ma061911h

34. Y. Qin, V. Litvinov, W. Chassé, B. Zhang, Y. Men, Change of lamellar morphology upon polymorphic transition of form II to form I crystals in isotactic polybutene-1 and its copolymer. Polymer **215**, 123355 (2021). https://doi.org/10.1016/j.polymer.2020.123355
35. F. Mellinger, M. Wilhelm, H.W. Spiess, R. Baumstark, A. Haunschild, Quantitative measurement of core coverage in core-shell particles by solid-state ^{1}H NMR spin-diffusion experiments. Macromol. Chem. Phys. **200**, 719–730 (1999). https://doi.org/10.1002/(SICI)1521-3935(19990401)200:4%3c719::AID-MACP719%3e3.0.CO;2-N
36. V.M. Litvinov, A.W.M. Braam, A.F.M.J. van der Ploeg, Telechelic ionomers: Molecular structure and kinetics of physical gelation of unsaturated polyester as studied by solid state NMR and X-ray. Macromolecules **34**, 489–502 (2001). https://doi.org/10.1021/ma001478q
37. Z. Lili, Q. Chen, E.W. Hansen, Morphology and phase characteristics of high-density polyethylene probed by NMR spin diffusion and second moment analysis. Macromol. Chem. Phys. **206**, 246–257 (2005). https://doi.org/10.1002/macp.200400343
38. C. Hedesiu, D.E. Demco, R. Kleppinger, G. Vanden Poel, W. Gijsbers, B. Blümich, K. Remerie, V.M. Litvinov, Effect of temperature and annealing on the phase composition, molecular mobility, and the thickness of domains in isotactic polypropylene studied by proton solid-state NMR, SAXS, and DSC. Macromolecules **40**, 3977–3989 (2007). https://doi.org/10.1021/ma070014q
39. M. Mauri, Y. Thomann, H. Schneider, K. Saalwächter, Spin-diffusion NMR at low field for the study of multiphase solids. Solid State Nucl. Magn. Res. **34**, 125–141 (2008). https://doi.org/10.1016/j.ssnmr.2008.07.001
40. F. Mellinger, M. Wilhelm, H.W. Spiess, Calibration of ^{1}H NMR spin diffusion coefficients for mobile polymers through transverse relaxation measurements. Macromolecules **32**, 4686–4691 (1999). https://doi.org/10.1021/ma9820265
41. C. Hedesiu, R. Kleppinger, D.E. Demco, A. Buda, B. Blümich, K. Remerie, V.M. Litvinov, The effect of temperature and annealing on the phase composition, molecular mobility and the thickness of domains in high-density polyethylene. Polymer **48**, 763–777 (2007). https://doi.org/10.1016/j.polymer.2006.12.019
42. W. Derbyshire, M. van den Bosch, D. van Dusschoten, W. MacNaughtan, I.A. Farhat, M.A. Hemminga, J.R. Mitchell, Fitting of the beat pattern observed in NMR free-induction decay signals of concentrated carbohydrate-water solutions. J. Magn. Reson. **168**, 278–283 (2004). https://doi.org/10.1016/j.jmr.2004.03.013
43. K. Schäler, M. Roos, P. Micke, Y. Golitsyn, A. Seidlitz, T. Thurn-Albrecht, H. Schneider, G. Hempel, K. Saalwächter, Basic principles of static proton low-resolution spin diffusion NMR in nanophase-separated materials with mobility contrast. Solid State Nucl. Magn. Res. **72**, 50–63 (2015). https://doi.org/10.1016/j.ssnmr.2015.09.001
44. X. Jia, J. Wolak, X. Wang, J.L. White, Independent calibration of 1H spin-diffusion coefficients in amorphous polymers by intramolecular polarization transfer. Macromolecules **36**, 712–718 (2003). https://doi.org/10.1021/ma0215316
45. M.E. Halse, A. Zagdoun, J.-N. Dumez, L. Emsley, Macroscopic nuclear spin diffusion constants of rotating polycrystalline solids from first-principles simulation. J. Magn. Reson. **254**, 48–55 (2015). https://doi.org/10.1016/j.jmr.2015.02.016
46. M.A. Voda, D.E. Demco, A. Voda, T. Schauber, M. Adler, T. Dabisch, A. Adams, M. Baias, B. Blümich, Morphology of thermoplastic polyurethanes by ^{1}H spin-diffusion NMR. Macromolecules **39**(14), 4802–4810 (2006). https://doi.org/10.1021/ma060335m
47. C. Melian, D.E. Demco, M. Istrate, A. Balaceanu, D. Moldovan, R. Fechete, C. Popescu, M. Möller, Morphology and side-chain dynamics in hydrated hard α-keratin fibers by ^{1}H solid-state NMR. Chem. Phys. Lett. **480**, 300–304 (2009). https://doi.org/10.1016/j.cplett.2009.09.013
48. D.L. VanderHart, G.B. McFadden, Some perspectives on the interpretation of proton NMR spin diffusion data in terms of polymer morphologies. Solid State Nucl. Magn. Res. **7**, 45–66 (1996). https://doi.org/10.1016/0926-2040(96)01233-7
49. T.T.P. Cheung, Effects of disorder in polymer morphology on spin diffusion. J. Phys. Chem. B **103**, 9423–9431 (1999). https://doi.org/10.1021/jp9906684
50. E.G. Sorte, A.L. Frischknecht, T.M. Alam, NMR spin diffusion measurements in disordered polymers: insights and limitations. Phys. Rev. Mater. **3**, 045602 (2019). https://doi.org/10.1103/PhysRevMaterials.3.045602
51. M. Roos, K. Schäler, A. Seidlitz, T. Thurn-Albrecht, K. Saalwächter, NMR study of interphase structure in layered polymer morphologies with mobility contrast: disorder and confinement effects vs. dynamic heterogeneities. Coll. Polym. Sci. **292**, 1825–1839 (2014). https://doi.org/10.1007/s00396-014-3218-8

52. H. Schneider, M. Roos, Y. Golitsyn, K. Steiner, K. Saalwächter, Dynamic heterogeneity of filler-associated interphases in polymer nanocomposites. Macromol. Rapid Com. **42**, 2100061 (2021). https://doi.org/10.1002/marc.202100061
53. V.M. Litvinov, B.D. Lavrukhin, A.A. Zhdanov, K.A. Andrianov, The effect of spin diffusion on the longitudinal nuclear magnetic relaxation for semicrystalline poly(dimethylsiloxane). Polym. Sci. USSR **20**, 2758–2768 (1978). https://doi.org/10.1016/0032-3950(78)90457-4
54. A.M. Kenwright, K.J. Packer, B.J. Say, Numerical simulations of the effects of spin-diffusion on NMR spin-lattice relaxation in semicrystalline polymers. J. Magn. Res. **69**, 426–439 (1986). https://doi.org/10.1016/0022-2364(86)90155-1
55. S. Zhang, M. Mehring, A modified Goldman-Shen NMR pulse sequence. Chem. Phys. Lett. **160**, 644–646 (1989). https://doi.org/10.1016/0009-2614(89)80079-X
56. A.M. Kenwright, B.J. Say, Analysis of spin-diffusion measurements by iterative optimization of numerical models. Solid State Nucl. Magn. Res. **7**, 85–93 (1996). https://doi.org/10.1016/S0926-2040(96)01251-9
57. V.M. Litvinov, Diffusivity of water molecules in amorphous phase of Nylon 6 fibers. Macromolecules **48**, 4748–4753 (2015). https://doi.org/10.1021/acs.macromol.5b00570
58. V. M. Litvinov. Molecular mobility and phase composition in polyolefins: from fundamental to applied research, in NMR Spectroscopy of Polymers: Innovative Strategies for Complex Macromolecules, ACS Symposium Series, Vol. 1077, ed. By H. N. Cheng, T. Asakura, A. D. English, ACS Symp. Series, (ACS, Washington, DC, 2011, ISBN 9780841226678, pp. 179–190. https://doi.org/10.1021/bk-2011-1077.ch011
59. V. Litvinov, Y. Men, Time-domain NMR in polyolefin research. Polymer **256**, 125205 (2022). https://doi.org/10.1016/j.polymer.2022.125205
60. C. Hedesiu, D.E. Demco, R. Kleppinger, G. Vanden Poel, K. Remerie, V.M. Litvinov, B. Blümich, R. Steenbakkers, Aging effects on the phase composition and chain mobility in isotactic poly(propylene). Macromol. Mater. Eng. **293**, 847–857 (2008). https://doi.org/10.1002/mame.200800140
61. V.M. Litvinov, J.P. Penning, Phase composition and molecular mobility in Nylon 6 fibers as studied by proton NMR transverse magnetisation relaxation. Macromol. Chem. Phys. **205**, 1721–1734 (2004). https://doi.org/10.1002/macp.200400089
62. R.R. Eckman, P.M. Henrichs, A.J. Peacock, Study of polyethylene by solid state NMR relaxation and spin diffusion. Macromolecules **30**, 2474–2481 (1997). https://doi.org/10.1021/ma9516753
63. S. Gautman, S. Balijepalli, G.C. Rutledge, Molecular simulations of the interlamellar phase in polymers: effect of chain tilt. Macromolecules **33**, 9136–9145 (2000). https://doi.org/10.1021/ma0012503
64. K. Tashiro, J. Hu, H. Wang, M. Hanesaka, A. Saiani, Refinement of the crystal structures of forms I and II of isotactic polybutene-1 and a proposal of phase transition mechanism between them. Macromolecules **49**, 1392–1404 (2016). https://doi.org/10.1021/acs.macromol.5b02785
65. W.-G. Hu, K. Schmidt-Rohr, Polymer ultradrawability: the crucial role of a-relaxation chain mobility in the crystallites. Acta Polym. **50**, 271–285 (1999). https://doi.org/10.1002/(SICI)1521-4044(19990801)50:8%3C271::AID-APOL271%3E3.0.CO;2-Y
66. K. Schmidt-Rohr, H.W. Spiess, Chain diffusion between crystalline and amorphous regions in polyethylene detected by 2D exchange carbon-13 NMR. Macromolecules **24**, 5288–5293 (1991). https://doi.org/10.1021/ma00019a011
67. D. Schaefer, H.W. Spiess, U.W. Suter, W.W. Fleming, Two-dimensional solid-state NMR studies of ultraslow chain motion: glass Transition in atactic poly(propy1ene) versus helical jumps in isotactic poly(propy1ene). Macromolecules **23**, 3431–3439 (1990). https://doi.org/10.1021/ma00216a008
68. T. Miyoshi, A. Mamum, D. Reichert, Fast dynamics and conformations of polymer in a conformational disordered crystal characterized by ^{1}H–^{13}C WISE NMR. Macromolecules **43**, 3986–3989 (2010). https://doi.org/10.1021/ma901927m
69. M. Schulz, A. Seidlitz, R. Kurz, R. Barenwald, A. Petzold, K. Saalwächter, T. Thurn-Albrecht, The underestimated effect of intracrystalline chain dynamics on the morphology and stability of semicrystalline polymers. Macromolecules **51**, 8377–8385 (2018). https://doi.org/10.1021/acs.macromol.8b01102
70. V. Litvinov, R. Deblieck, C. Clair, W. Van den Fonteyne, A. Lallam, R. Kleppinger, D.A. Ivanov, M.E. Ries, M. Boerakker, Molecular structure, phase composition, melting behavior and chain entanglements in the amorphous phase of high-density polyethylenes. Macromolecules **53**, 5418–54133 (2020). https://doi.org/10.1021/acs.macromol.0c00956
71. I.C. Sanchez, J.P. Colson, R.K. Egy, Theory and observations of polymer crystal thickening. J. Appl. Phys. **44**, 4332–4339 (1973). https://doi.org/10.1063/1.1661961

72. D.E. Demco, V.M. Litvinov, G. Rata, C. Popescu, K.-H. Plan, A. Schmidt, B. Blümich, Investigation of thermal aging of polyamide 4,6 by ^{1}H solid-state NMR. Macromol. Chem. Phys. **208**, 2085–2095 (2007). https://doi.org/10.1002/macp.200700095
73. J.R. Havens, D.L. VanderHart, Morphology of polyethylene terephthalate) fibers as studied by multiple-pulse NMR. Macromolecules **18**, 1663–1676 (1985). https://doi.org/10.1021/ma00151a005
74. P. Smith, P.J. Lemstra, Ultra-high strength polyethylene filaments by solution spinning/drawing 3 Influence of drawing temperature. Polymer **21**, 1341–1343 (1980). https://doi.org/10.1016/0032-3861(80)90205-0
75. W.-G. Hu, K. Schmidt-Rohr, Characterization of ultradrawn polyethylene fibers by NMR: crystallinity, domain sizes and a highly mobile second amorphous phase. Polymer **41**, 2979–2987 (2000). https://doi.org/10.1016/S0032-3861(99)00429-2
76. D.E. Demco, C. Melian, J. Simmelink, V.M. Litvinov, M. Möller, Structure and dynamics of drawn gel-spun ultra-high molecular weight polyethylene fibers by ^{1}H, ^{13}C and ^{129}Xe NMR. Macromol. Chem. Phys. **211**, 2611–2623 (2010). https://doi.org/10.1002/macp.201000455
77. V.M. Litvinov, J. Xu, C. Melian, D.E. Demco, M. Möller, J. Simmelink, Morphology, chain dynamics and domain sizes in gel-spun ultra-high molecular weight polyethylene fibers at final stages of drawing by SAXS, WAXS and ^{1}H solid-state NMR. Macromolecules **44**, 9254–9266 (2011). https://doi.org/10.1021/ma201888f
78. V.M. Litvinov, M.E. Ries, A. Henke, P. Matloka, T. Baughman, Chain entanglements in polyethylenes melts. Why it is studied again? Macromolecules **46**, 541–547 (2013). https://doi.org/10.1021/ma302394j
79. V.M. Litvinov, R.A. Orza, M. Klüppel, M. van Duin, P.C.M.M. Magusin, Rubber—filler interactions and network structure in relation to stress–strain behaviour of vulcanized, carbon black filled EPDM. Macromolecules **44**, 4887–4900 (2011). https://doi.org/10.1021/ma2007255
80. J.C. Kenny, V.J. McBrierty, Z. Rigbi, D.C. Douglass, Carbon black filled natural rubber. 1. Structural investigations. Macromolecules **24**(2), 436–443 (1991). https://doi.org/10.1021/ma00002a015
81. V.M. Litvinov, P.A.M. Steeman, EPDM-carbon black interactions and the reinforcement mechanisms, as studied by low-resolution ^{1}H NMR. Macromolecules **32**, 8476–8490 (1999). https://doi.org/10.1021/ma9910080
82. J.W. ten Brinke, V.M. Litvinov, J.E.G.J. Wijnhoven, J.W.M. Noordermeer, Interactions of stöber silica with natural rubber under the influence of coupling agents, studied by ^{1}H NMR T_2 relaxation analysis. Macromolecules **35**, 10026–10037 (2002). https://doi.org/10.1021/ma020555+
83. V. M. Litvinov, A. A. Zhdanov. NMR study of the polymer-filler interactions. In: *Doklady Phys. Chem.: Proceedings of the Academy of Sciences of the USSR 283*, 811–814 (1985).
84. V. M. Litvinov, Poly(dimethylsiloxane) Chains at a Silica Surface, in *Organosilicon Chemistry II. From Molecules to Materials*, ed. By N. Auner, J. Weis, (Wiley, Weinheim, 1996) pp. 779–814. (ISBN:9783527292547)
85. V.J. McBrierty, J.C. Kenny, Structural investigations of carbon black-filled elastomers using NMR and ESR. Kautsch. Gummi Kunstst. **47**, 342–348 (1994)
86. G. Leu, Y. Liu, D.D. Werstler, D.G. Cory, NMR characterization of elastomer−carbon black interactions. Macromolecules **37**, 6883–6891 (2004). https://doi.org/10.1021/ma0493628
87. J.F. Schenck, The role of magnetic susceptibility in magnetic resonance imaging: MRI magnetic compatibility of the first and second kinds. Med. Phys. **23**, 815–850 (1996). https://doi.org/10.1118/1.597854
88. M.E.L. Wouters, V.M. Litvinov, F.L. Binsbergen, J.G.P. Goossens, M. van Duin, H.G. Dikland, Morphology of ethylene-propylene copolymers based ionomers as studied by solid state NMR and small angle X-ray scattering in relation to some mechanical properties. Macromolecules **36**, 1147–1156 (2003). https://doi.org/10.1021/ma020358a

Authors and Affiliations

V. M. Litvinov[1,2] · Yongfeng Men[2,3]

✉ V. M. Litvinov
V.LIT.CON@kpnmail.nl

[1] V.Lit.Consult, Gozewijnstraat 4, 6191 WV Beek, The Netherlands

[2] State Key Laboratory of Polymer Physics and Chemistry, Changchun Institute of Applied Chemistry, Chinese Academy of Sciences, Renmin Street 5625, Changchun 130022, People's Republic of China

[3] School of Applied Chemistry and Engineering, University of Science and Technology of China, Hefei 230026, People's Republic of China